International Journal of Plasticity 178 (2024) 104013

Contents lists available at ScienceDirect

International Journal of Plasticity

journal homepage: www.elsevier.com/locate/ijplas

Restraining geometrically-necessary dislocations to the active slip systems in a crystal plasticity-based finite element framework

Eralp Demir [a,*], Alvaro Martinez-Pechero [a,b], Chris Hardie [b], Edmund Tarleton [a]

[a] Department of Engineering Science, University of Oxford, Parks road, Oxford OX1 3PJ, UK
[b] UK Atomic Energy Authority, Culham Science Centre, Abingdon, Oxfordshire, OX14 3DB, UK

ARTICLE INFO

Dataset link: https://github.com/TarletonGroup/CrystalPlasticity

Keywords:
GND restricted to active slip systems
Singular value decomposition
GND density threshold
Crystal plasticity

ABSTRACT

Strain gradients have been cast in the form of geometrically-necessary dislocations (GND) to relate the length-scale dependence of strength and to determine potential sites for failure initiation. The literature contains various different incompatibility measures, the main ones being: the total form ($\nabla \times \boldsymbol{F}_p$), the rate form for large displacements ($\nabla \times \dot{\gamma}^a \boldsymbol{n}^a \boldsymbol{F}_p$), and the slip gradient form ($\nabla \dot{\gamma}^a$). Here, these different approaches are compared rigorously for the first time. Obtaining GND densities when using the total form is a rank-deficit linear problem, solved by singular value decomposition (SVD) known as the Least Squares Minimization (L2 method). Alternative methods for finding GND densities such as Karush–Kuhn–Tucker (KKT) optimization are also investigated. Both L2 and KKT methods predict unrealistic GND densities on inactive slip systems leading to excessive strain hardening; even for a single crystal single slip case. Therefore, the restriction of GNDs to the active slip systems by using a threshold based on the total slip is proposed. This restriction reveals relatively consistent results for various single crystal single slip cases including: simple shear, uniaxial tension, and four-point bending. In addition, the small numerical differences in the slip leads to large discrepancies in the flow stress due to error accumulation, even for strain-gradient-free uniaxial tension, hence a threshold for the GND density increment (2×10^2 m^{-2}) is used in all models to avoid formation of erroneous GND densities. Finally, the proposed method is applied to the evolution of the GND density for a grain inside a polycrystal aggregate that posses a complex stress state. The lowest incompatibility error is obtained by both of the total forms that use the curl of the plastic deformation gradient with the active slip system restriction suggesting them to be the most reliable GND measures.

1. Introduction

Strain gradients have been used to account for the length scale dependence of mechanical strength with various physical origins (Fleck et al., 1994). GND and strain gradients were used to explain various physical phenomena. For example, GNDs were used to reveal the crack initiation and strain localization sites in a single crystal (Prastiti et al., 2020) and in polycrystals (Chen et al., 2017). Polycrystal applications include modeling the Hall–Petch grain size effect (Counts et al., 2008), length scale effect in multi-phase steels (Lyu et al., 2015) and martensitic steels (Sun et al., 2019), understanding shear localization in high-purity titanium (Zhu et al., 2017), creep in nickel-based superalloy (Birosca et al., 2019), transformation induced defect formations in dual-phase steels (Ramazani et al., 2013), tension–compression asymmetry in an aluminum alloy (Sun et al., 2022), and modeling of indentation of ion-irradiated materials (Xiao et al., 2019).

* Corresponding author.
E-mail address: eralp.demir@eng.ox.ac.uk (E. Demir).

https://doi.org/10.1016/j.ijplas.2024.104013
Received 21 December 2023; Received in revised form 30 April 2024
Available online 23 May 2024

Table 1
Incompatibility measures used in the literature. $\nabla\times$ represents the curl applied to the deformation fields such as plastic part of the deformation, $\boldsymbol{F}_p$, elastic deformation gradient, $\boldsymbol{F}_e$, dislocation tensor, $\boldsymbol{G}$, total slip, γ^a, rotations, $\boldsymbol{g}$ and elastic strains $\boldsymbol{\epsilon}_e$. The incompatibility measures are shown for illustration purposes only, the exact measures could be found in the corresponding references.

Incompatibility	References
$\nabla \times \boldsymbol{F}_p$	Dai (1997), Dunne et al. (2007), Das et al. (2018), Kuksenko et al. (2019), Bandyopadhyay et al. (2021), Xu (2021a), Sedaghat and Abdolvand (2021)
$\boldsymbol{F}_p \left(\nabla \times \boldsymbol{F}_p\right)$	Cermelli and Gurtin (2001), Counts et al. (2008)
$\nabla \times \left(\dot{\gamma}^a \boldsymbol{n}^a \boldsymbol{F}_p\right)$	Dai (1997), Ma et al. (2006), Busso et al. (2000), Counts et al. (2008), Sun et al. (2022)
$\nabla \gamma^a$	Dai (1997), Gerken and Dawson (2008), Klusemann and Yalçinkaya (2013), Xiao et al. (2019)
$\nabla \times \boldsymbol{F}_e^{-1}$	Acharya and Bassani (2000), Clayton et al. (2004)
$\nabla \times \boldsymbol{g}$	Arsenlis and Parks (1999), El-Dasher et al. (2003), Pantleon (2008), Demir et al. (2009), Konijnenberg et al. (2015), Witzen et al. (2020)
$\nabla \times \left(\boldsymbol{g} + \boldsymbol{\epsilon}_e\right)$	Wilkinson et al. (2006), Jiang et al. (2015)
$\boldsymbol{F}_p \frac{\partial}{\partial t}\left(\boldsymbol{F}_p^{-1} \boldsymbol{G} \boldsymbol{F}_p^{-T}\right) \boldsymbol{F}_p^T$	Cermelli and Gurtin (2001), Stupkiewicz and Petryk (2016)

The heterogeneity in plastic deformation has been expressed in terms of the geometrically-necessary dislocation (GND) density, ϱ_{GND}, which is the length of dislocations per unit volume. Similarly, the statistically-stored dislocation density, ϱ_{SSD}, accounts for dislocations with a net Burgers vector of zero. Dislocations contribute to the strength by Taylor's relation, $\tau_c = \alpha G b \sqrt{\varrho_{GND} + \varrho_{SSD}}$), where α, G, b, and τ_c represent geometrical factor, shear modulus, Burgers vector, and slip strength.

The total deformation in a crystal is compatible unless there exists voids or gaps in the material. Therefore, either the plastic or elastic deformation has been used to quantify the lattice incompatibility (Arsenlis and Parks, 1999). Elastic distortion consists of rotation and elastic strain parts, both of which can be determined experimentally using electron backscattered diffraction (EBSD) measurements (Wilkinson et al., 2006). Therefore, many studies used orientation gradients to quantify GNDs from experimentally obtained EBSD maps (Demir et al., 2009; Konijnenberg et al., 2015; Witzen et al., 2020) while elastic strain gradients were also included in recent studies (Jiang et al., 2015). Although widely used, the L2 minimization method (Arsenlis and Parks, 1999) predicts GND densities at least an order of magnitude higher than the L1 minimization which was recently shown with a discretization based on finite element method (Demir et al., 2023a).

Numerical solution procedures lead to inaccuracies that may potentially cause instabilities in the GND calculations. To overcome the numerical instabilities, an analytical solution has been proposed to find the GND density (Kysar et al., 2010). Alternatively, a kernel based GND calculation method instead of an elemental calculation procedure has reduced the mesh sensitivity of GND density (Xu, 2021a). Similarly, mesh-free methods were used to compute the gradient field rather than using conventional finite element shape functions (Zhang and Dong, 2015; Tang et al., 2023).

Higher order theories introduced micro stress as another field variable (Gurtin, 2000). In these theories, the GND density was treated as a separate field variable to search for a simultaneous solution with mechanical equilibrium (Evers et al., 2004; Kuroda and Tvergaard, 2008). Second order theories demand for additional boundary conditions such as micro-hard grain boundaries (Pouriayevali and Xu, 2017) which are indeed experimentally not yet validated. Therefore, various forms of first order strain gradient theory and finite element-based calculations have still been used widely as a simple means to introduce length-scale dependence avoiding making assumptions about the grain boundary behavior, which is known to be very complex (Zan et al., 2023; Pai et al., 2022; Li et al., 2023; Gao et al., 2023). Similarly, micromorphic theories demand for calculation of higher order gradients which is solved by using a separate field solver for the micromorphic variable (Ryś et al., 2020).

Dislocation flux has been used as an alternative measure to compute the strain gradients (Roters et al., 2012). However, flux computation relies on area integrals hence it is equivalent to using a volume integral using the divergence theorem (Reuber et al., 2014). Accordingly, the conventional volume-based strain gradient computations are performed elementally instead of an inter-elemental approach in flux models. The latter introduces additional complexity for a polycrystal case with grain boundaries, for example additional probability functions to quantify the slip transfer between two grains at a grain boundary (Zhang et al., 2023).

Table 1 shows different incompatibility measures used to compute GND densities which were adopted in various studies. Computational approaches have the freedom to use various measures for incompatibility while the experimental measurements are limited to rotations from the orientation changes and elastic strains as the currently available methods.

This study overviews first order strain gradient computation procedures that aims at finding an accurate measure for GND density. The numerical procedures are susceptible to produce errors, hence the error sources need to be identified. For example, the widely used least squares solution known as the L2-minimum (Arsenlis and Parks, 1999) reveals GNDs on the inactive slip systems. Similarly, time integration causes error accumulation that appear as erratic GND densities at smaller dimensions. For this reason, various strain gradient approaches are investigated, including the different variants of the curl of $\boldsymbol{F}_p$ such as the rate form originally proposed in Dai (1997), and slip gradients. Comparison of GND distributions for different boundary conditions including simple shear, uniaxial tension, and bending are performed for various 2D and 3D element types with quadrilateral and linear interpolation functions in order to identify important constraints that are needed to accurately represent GND densities. Finally the lattice incompatibility error is quantitatively determined for different GND measures using a realistic polycrystal scenario.

2. Modeling

A brief overview of crystal plasticity kinematics is presented followed by constitutive models and the numerical solution method[1]. Next, the derivations for different strain gradient models are revisited in detail to provide a complete reference. Strain gradient explanations include overview of fundamental definitions: Burgers circuit and four different lattice incompatibility measures including two total forms, a time rate form, and a slip gradient form.

2.1. Crystal plasticity kinematics

The total deformation gradient, $\boldsymbol{F}$, is multiplicatively decomposed into its elastic, $\boldsymbol{F}_e$, and plastic parts, $\boldsymbol{F}_p$ with volume remaining constant during plastic deformation:

$$\boldsymbol{F} = \boldsymbol{F}_e \boldsymbol{F}_p, \quad \det(\boldsymbol{F}_p) = 1. \tag{2.1}$$

The plastic velocity gradient is obtained by the sum of the slip rates with the dyadic product of slip direction, $\boldsymbol{s}^a$, and slip plane normal, $\boldsymbol{n}^a$, in the intermediate configuration[2]:

$$\boldsymbol{L}_p = \sum_a \dot{\gamma}^a \boldsymbol{s}^a \otimes \boldsymbol{n}^a. \tag{2.2}$$

Slip direction and slip plane normal transform to the deformed reference that is indicated with the subscript e as:

$$\boldsymbol{s}_e^a = \boldsymbol{F}_e \boldsymbol{s}^a, \quad \boldsymbol{n}_e^a = \boldsymbol{F}_e^{-T} \boldsymbol{n}^a. \tag{2.3}$$

The total velocity gradient is given by:

$$\boldsymbol{L} = \dot{\boldsymbol{F}} \boldsymbol{F}^{-1}. \tag{2.4}$$

The total velocity gradient can be expressed as the sum of symmetric stretch rate (or rate of deformation), $\boldsymbol{D}$, and anti-symmetric spin tensors, $\boldsymbol{\Omega}$:

$$\boldsymbol{L} = \boldsymbol{D} + \boldsymbol{\Omega}. \tag{2.5}$$

The total strain rate can be decomposed into its elastic and plastic parts:

$$\boldsymbol{D} = \boldsymbol{D}_e + \boldsymbol{D}_p. \tag{2.6}$$

The total slip per slip system is obtained by the net sum of slip rates over time up to the current time step which is indicated by former time, t, plus the time step, Δt, in incremental solutions:

$$\gamma^a = \int_0^{t+\Delta t} \dot{\gamma}^a \, \mathrm{d}t. \tag{2.7}$$

2.2. Constitutive laws

Elasticity relates the rotation-free objective Jaumann rate of stress, $\overset{\nabla}{\boldsymbol{\sigma}}_e$, to the vectorized form of elastic deformation rate in Voigt notation, $\boldsymbol{d}_e$. The subscript e stands for the configuration changes due to elastic deformation. According to Hill and Rice (1972):

$$\overset{\nabla}{\boldsymbol{\sigma}}_e \approx \boldsymbol{C} \cdot \boldsymbol{d}_e. \tag{2.8}$$

$\boldsymbol{C}$ is the (6×6) matrix of elastic constants in the deformed configuration which is obtained by transforming the single crystal stiffness matrix, $\boldsymbol{C}_0$, from the crystal reference to the sample or deformed reference using:

$$\boldsymbol{C} = \boldsymbol{R} \boldsymbol{C}_0 \boldsymbol{R}^T. \tag{2.9}$$

$\boldsymbol{R}$ is a (6×6) special transformation matrix that is constructed to transform the matrix of elastic stiffness constants in Voigt notation (Bond, 1943) which uses components of the crystal to sample transformation matrix, $\boldsymbol{g}$:

$$\boldsymbol{R} = \begin{bmatrix} (g_{11})^2 & (g_{12})^2 & (g_{13})^2 & 2\,g_{11}\,g_{12} & 2\,g_{13}\,g_{11} & 2\,g_{12}\,g_{13} \\ (g_{21})^2 & (g_{22})^2 & (g_{23})^2 & 2\,g_{21}\,g_{22} & 2\,g_{23}\,g_{21} & 2\,g_{22}\,g_{23} \\ (g_{31})^2 & (g_{32})^2 & (g_{33})^2 & 2\,g_{31}\,g_{32} & 2\,g_{33}\,g_{31} & 2\,g_{32}\,g_{33} \\ g_{11}\,g_{21} & g_{12}\,g_{22} & g_{13}\,g_{23} & g_{11}\,g_{22}+g_{12}\,g_{21} & g_{13}\,g_{21}+g_{11}\,g_{23} & g_{12}\,g_{23}+g_{13}\,g_{22} \\ g_{31}\,g_{11} & g_{32}\,g_{12} & g_{33}\,g_{13} & g_{11}\,g_{32}+g_{12}\,g_{31} & g_{13}\,g_{31}+g_{11}\,g_{33} & g_{12}\,g_{33}+g_{13}\,g_{32} \\ g_{21}\,g_{31} & g_{22}\,g_{32} & g_{23}\,g_{33} & g_{22}\,g_{31}+g_{21}\,g_{32} & g_{21}\,g_{33}+g_{23}\,g_{31} & g_{22}\,g_{33}+g_{23}\,g_{32} \end{bmatrix}. \tag{2.10}$$

[1] The fourth rank tensors are shown with $\mathbb{A}$ or A_{ijkl}, second rank tensors are with capital letters in bold fonts, $\boldsymbol{A}$ or A_{ij}, vectors with small letters in bold fonts, $\boldsymbol{a}$ or a_i, and scalars with regular fonts, a, throughout this study.

[2] Intermediate of relaxed configuration is a nonphysical reference frame to account for the shape changes after slip, $\boldsymbol{F}_p$.

Different from conventional literature, the transformation matrix $\boldsymbol{g}$ maps the crystal reference to the material orientation in the deformed configuration, which initially (at $t = 0$) can be defined in terms of the Bunge angles as shown in Appendix A.

The stiffness in the crystal reference is given by Eq. (2.11) for a cubic material with three independent elastic constants C_{11}, C_{12}, and C_{44}:

$$\boldsymbol{C}_0 = \begin{bmatrix} C_{11} & C_{12} & C_{12} & 0 & 0 & 0 \\ C_{12} & C_{11} & C_{12} & 0 & 0 & 0 \\ C_{12} & C_{12} & C_{11} & 0 & 0 & 0 \\ 0 & 0 & 0 & C_{44} & 0 & 0 \\ 0 & 0 & 0 & 0 & C_{44} & 0 \\ 0 & 0 & 0 & 0 & 0 & C_{44} \end{bmatrix}. \tag{2.11}$$

The slip rates are computed by Eq. (2.12) (Power law slip (Asaro, 1983)) using a reference slip rate, $\dot{\gamma}_0$, and a rate sensitivity exponent, n:

$$\dot{\gamma}^a = \dot{\gamma}_0 \left(|\tau^a| / \tau_c^a \right)^n \operatorname{sgn}(\tau^a). \tag{2.12}$$

Taylor's relation in Eq. (2.13) is used to compute the critical resolved shear stress on slip system a (τ_c^a) in which τ_c^0, α, G, b^a, and ϱ_{for}^a represent the lattice friction, geometric factor, shear modulus, Burgers vector, and forest dislocation density, respectively. Statistically-stored dislocations (Ruggles et al., 2016) are ignored in this study to investigate the direct effect of GNDs only on strength:

$$\tau_c^a = \tau_c^0 + \alpha\, G\, b \sqrt{\varrho_{for}^a}. \tag{2.13}$$

Strain hardening due to the dislocation interactions are known to be present. The forest projections of dislocations to other systems is assumed to account for these interactions. Therefore, forest dislocation density is computed using projection of edge, $\varrho_{GND,e}^b$, and screw $\varrho_{GND,s}^b$ type of GND densities onto the slip plane normals:

$$\varrho_{for}^a = \sum_b \left| \boldsymbol{n}^a \cdot \boldsymbol{t}^b \right| \left| \varrho_{GND,e}^b \right| + \left| \boldsymbol{n}^a \cdot \boldsymbol{s}^b \right| \left| \varrho_{GND,s}^b \right|, \tag{2.14}$$

where $\boldsymbol{t}^b$ is the cross product of slip direction and slip plane normal:

$$\boldsymbol{t}^b = \boldsymbol{s}^b \times \boldsymbol{n}^b. \tag{2.15}$$

2.3. Strain-gradient models

Total form, rate form, and small strain measures are investigated that are all based on the plastic part of the deformation gradient. For the total form, the solution for GND densities is obtained by four different methods including; L2 minimization (giving the minimum dislocation line length), the Karush–Kuhn–Tucker (KKT) optimality condition, the solution for GND densities restricted to active slip systems only, and finally the same restricted solution with an additional correction accounting for geometrical changes due to plastic deformation.

The curl of a second rank tensor is computed according to Eq. (2.16) in which ε_{irs} represents the Levi-Civita symbol. This corresponds to the same curl definition as in Cermelli and Gurtin (2001) and the "curl3" definition in Das et al. (2018). The derivation of Eq. (2.16) is revisited in Appendix B:

$$(\nabla \times \boldsymbol{T})_{ij} = \varepsilon_{irs}\, T_{js,r}. \tag{2.16}$$

2.3.1. Burgers circuit

The Burgers circuit is defined here to indicate the sign conventions of dislocations for a given slip gradient in a deforming single crystal lattice. Compatibility is satisfied for the total deformation in the deformed configuration, thus incompatibility of plastic deformation is calculated by the Burgers circuit that belong to the intermediate or microstructural configuration.

Fig. 1 shows the Burgers circuit around edge and screw type dislocations. A positive shear gradient for a single slip case is accommodated by a negative edge dislocation, Fig. 1(a) and a positive shear gradient leading to a negative left-handed screw dislocation (Hull and Bacon, 2011), Fig. 1(b).

The Burgers circuit is a line integral about the loop C, revealing the net closure failure, $\boldsymbol{b}_{net}$, for a plastically-deformed lattice in terms of the deformed vectors at the intermediate configuration, $\boldsymbol{Y}$, as shown in Eq. (2.17):

$$\boldsymbol{b}_{net} = -\oint_C \mathrm{d}\boldsymbol{Y}. \tag{2.17}$$

The same incompatibility can be computed in the undeformed configuration, C_0 in terms of the undeformed vectors, $\boldsymbol{X}_0$, by change of basis[3]:

$$\boldsymbol{b}_{net} = -\oint_{C_0} \boldsymbol{F}_p\, \mathrm{d}\boldsymbol{X}_0. \tag{2.18}$$

[3] The quantities at the undeformed lattice are denoted with the subscript 0.

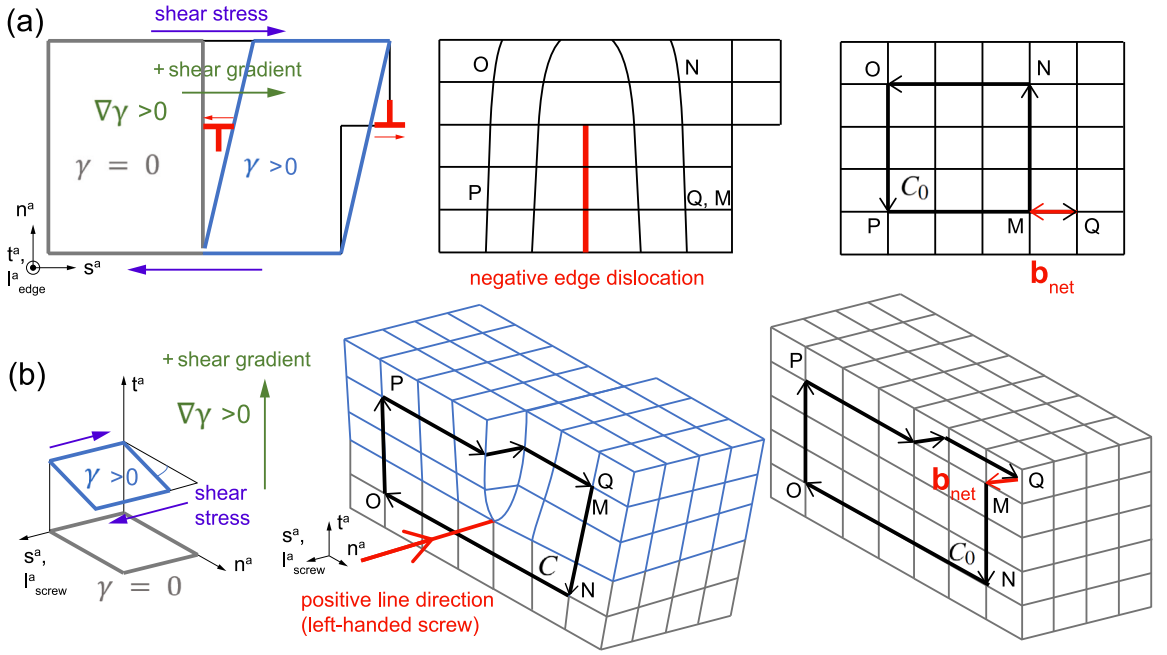

Fig. 1. GND sign convention for a positive shear gradient, $+\nabla\gamma$, resulting in a (a) negative edge dislocation and (b) negative screw dislocation (left-handed screw). The Burger's circuits are indicated with the set of points M-N-O-P-Q with the net Burger's vectors of $\boldsymbol{b}_{net}$ anti-parallel to the line direction. $\gamma > 0$ and $\gamma = 0$ represent the sheared and unsheared portions of the lattice.

$\boldsymbol{F}_p$ maps the undeformed vectors, $\mathrm{d}\boldsymbol{X}_0$, to the intermediate or microstructural configuration with:

$$\mathrm{d}\boldsymbol{Y} = \boldsymbol{F}_p\,\mathrm{d}\boldsymbol{X}_0. \tag{2.19}$$

Using Stokes theorem, the line integral is converted to an area integral with the area normal $\boldsymbol{r}_0$ and curl operation as:

$$\boldsymbol{b}_{net} = -\int_{S_0} \left(\nabla \times \boldsymbol{F}_p\right)^T \cdot \boldsymbol{r}_0\,\mathrm{d}S_0. \tag{2.20}$$

Alternatively, Cermelli and Gurtin (2001) expresses a different form of incompatibility by considering the changes in the area normals with plastic deformation in the integral Eq. (2.20) at the microstructural configuration using the change of basis according to Nanson's relation ($\boldsymbol{r}\,\mathrm{d}S = \det(\boldsymbol{F})\,\boldsymbol{F}^{-T}\,\boldsymbol{r}_0\,\mathrm{d}S_0$) and considering isochoric plasticity ($\det(\boldsymbol{F}_p) = 1$) which takes the form:

$$\boldsymbol{b}_{net} = -\int_{S} \left(\nabla \times \boldsymbol{F}_p\right)^T \cdot \boldsymbol{F}_p^T\,\boldsymbol{r}\,\mathrm{d}S. \tag{2.21}$$

2.3.2. Nye tensor

The lattice incompatibility needs to be fulfilled by dislocations that are called geometrically-necessary dislocations (GNDs) unless there is a discontinuity like a crack or void. Nye defined the dislocation tensor as the dislocation lines, $\boldsymbol{l}^a$, that pierce through an arbitrary area normal, $\boldsymbol{r}$, contributing as much as their projected Burgers vector, b^a, Nye (1953) as schematically shown in Fig. 2. Note that the line direction is along the slip direction, $\boldsymbol{s}^a$ for a screw and it along the transverse direction, $\boldsymbol{t}^a$, for an edge, giving a net Burgers vector of $\boldsymbol{b}_{net}$ at the microstructural configuration:

$$\boldsymbol{b}_{net} = \int_S \left(\sum_a \varrho^a_{GND}\, b^a\, \boldsymbol{s}^a \otimes \boldsymbol{l}^a\right) \cdot \boldsymbol{r}\,\mathrm{d}S. \tag{2.22}$$

2.3.3. Total form

The incompatibility measure obtained from the Burgers circuit, Eq. (2.20), shall be satisfied by Nye's tensor in Eq. (2.22) which gives:

$$\boldsymbol{b}_{net} = -\int_{S_0} \left(\nabla \times \boldsymbol{F}_p\right)^T \cdot \boldsymbol{r}_0\mathrm{d}S_0 = \int_S \left(\sum_a \varrho^a_{GND}\, b^a\, \boldsymbol{s}^a \otimes \boldsymbol{l}^a\right) \cdot \boldsymbol{r}\,\mathrm{d}S. \tag{2.23}$$

Ignoring the changes in the area with plastic deformation ($\boldsymbol{r}_0\mathrm{d}S_0 = \boldsymbol{r}\,\mathrm{d}S$) and canceling out the integrals on both sides, gives the overall incompatibility measure as:

$$\boldsymbol{\Lambda} = -\left(\nabla \times \boldsymbol{F}_p\right)^T = \sum_a \varrho^a_{GND}\, b^a\, \boldsymbol{s}^a \otimes \boldsymbol{l}^a, \tag{2.24}$$

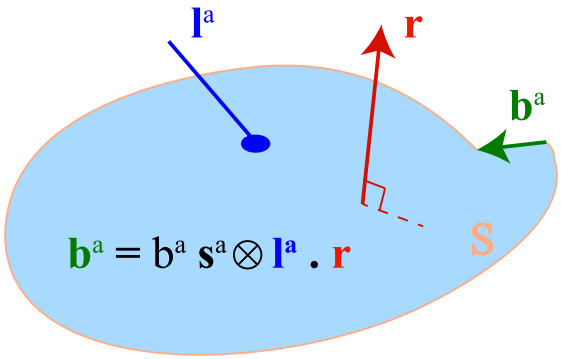

Fig. 2. A dislocation line, l^a, penetrating through an arbitrary area normal, $\boldsymbol{r}$, of a surface S at the microstructural or intermediate configuration.

Eq. (2.25) shows the same expression in index notation, note the negative sign and the transpose to match the dislocation convention of Nye's tensor:

$$\Lambda_{ji} = -\varepsilon_{irs} F_{p_{js,r}} = \sum_a \varrho^a_{GND}\, b^a\, s^a_j\, l^a_i. \tag{2.25}$$

Considering changes in the area normal or the dislocation flux (Cermelli and Gurtin, 2001):

Alternatively, the changes in the area normal vector and the area shall be considered for large deformations as in Eq. (2.21). Therefore, setting the incompatibility measure equal to Nye's tensor in Eq. (2.22) gives:

$$\boldsymbol{b}_{net} = -\int_S \left(\nabla \times \boldsymbol{F}_p\right)^T \cdot \boldsymbol{F}_p^T \boldsymbol{r}\,\mathrm{d}S = \int_S \left(\sum_a \varrho^a_{GND}\, b^a\, \boldsymbol{s}^a \otimes \boldsymbol{l}^a\right) \cdot \boldsymbol{r}\,\mathrm{d}S. \tag{2.26}$$

Canceling out the integrals on both sides, gives the overall incompatibility measure in Eq. (2.27). A detailed derivation can also be found in Arora et al. (2020):

$$\boldsymbol{\Lambda}' = -\left(\nabla \times \boldsymbol{F}_p\right)^T \boldsymbol{F}_p^T = \sum_a \varrho^a_{GND}\, b^a\, \boldsymbol{s}^a \otimes \boldsymbol{l}^a, \tag{2.27}$$

or in index notation:

$$\Lambda'_{ji} = -\varepsilon_{mrs} F_{p_{js,r}} F_{pim} = \sum_a \varrho^a_{GND}\, b^a\, s^a_j\, l^a_i. \tag{2.28}$$

The incompatibility tensor can be written as the sum of dislocation families; screws and edges:

$$\boldsymbol{\Lambda} = \sum_a \varrho^a_{GND,e}\, b^a\, \boldsymbol{s}^a \otimes \boldsymbol{t}^a + \varrho^a_{GND,s}\, b^a\, \boldsymbol{s}^a \otimes \boldsymbol{s}^a. \tag{2.29}$$

Therefore, the solution for the dislocation densities, $\{\boldsymbol{\varrho}_{GND}\}$, of the linear problem in Eq. (2.30) is needed:

$$\{\boldsymbol{\Lambda}\} = [\boldsymbol{A}]\,\{\boldsymbol{\varrho}_{GND}\}. \tag{2.30}$$

For face-centered-cubic materials there are 18 dislocation densities; 12 edge and 6 screw dislocations. More dislocation families are present for bcc and hcp structures. However, the incompatibility tensor has 9 known components, the coefficient matrix, $[\boldsymbol{A}]$ therefore has a size of 9 by 18 for FCC materials, so the solution is not unique. In this paper, three different solution techniques for GND densities is investigated that are explained in the following (The solution method used for GND model 1-c and 1-d are the same but incompatibility measure is different.).

- **GND model 1-a:** L2 minimization
  The incompatibility measure for model 1-a is the total form that relies on the curl of the plastic deformation gradient, (2.24). The incompatibility accommodated by the GND geometry defined in the $[\boldsymbol{A}]$ matrix. Once the incompatibility is computed, the GND density is obtained by calculating the right-pseudo inverse of $\boldsymbol{A}$ (Das et al., 2018), which has full column rank ($r = 9$). This is equivalent to L2 minimization (Arsenlis and Parks, 1999), or least-squares fitting to solve Eq. (2.30). The inversion is necessary to solve for the linear equation which is underdetermined:

$$\{\boldsymbol{\varrho}_{GND}\} = [\boldsymbol{A}]^+\,\{\boldsymbol{\Lambda}\}. \tag{2.31}$$

  where,

$$[\boldsymbol{A}]^+ = [\boldsymbol{A}]^T \left([\boldsymbol{A}]\,[\boldsymbol{A}]^T\right)^{-1}. \tag{2.32}$$

- **GND model 1-b:** KKT optimization
  In this model, the total form of the incompatibility in Eq. (2.24) is used and minimized using KKT optimality criterion. The L2 functional, C, is defined as in Eq. (2.33), which is a function of GND density, $\boldsymbol{\varrho}_{GND}$, and a vector, λ, containing penalty factors of the Lagrange multiplier:

$$C(\boldsymbol{\varrho}_{GND}, \lambda) = \boldsymbol{\varrho}_{GND}^{T}\, \boldsymbol{\varrho}_{GND} + \lambda^{T} (\boldsymbol{A}\, \boldsymbol{\varrho}_{GND} - \boldsymbol{\Lambda}). \tag{2.33}$$

  The KKT optimality criteria gives:

$$\frac{\partial C(\boldsymbol{\varrho}_{GND}, \lambda)}{\partial \boldsymbol{\varrho}_{GND}} = \mathbf{0}. \tag{2.34}$$

$$\frac{\partial C(\boldsymbol{\varrho}_{GND}, \lambda)}{\partial \lambda} = \mathbf{0}. \tag{2.35}$$

  Substituting Eq. (2.35) into Eq. (2.33) gives:

$$2\boldsymbol{\varrho}_{GND} + \lambda^{T}\, \boldsymbol{A} = \mathbf{0}. \tag{2.36}$$

$$\boldsymbol{A}\, \boldsymbol{\varrho}_{GND} - \boldsymbol{\Lambda} = \mathbf{0}. \tag{2.37}$$

  Using the simple identity; $\lambda^{T}\, \boldsymbol{A} = \boldsymbol{A}^{T}\, \lambda$, the simulatenous solution for the GND densities and penalty parameters can be obtained as:

$$\begin{bmatrix} 2\boldsymbol{I} & \boldsymbol{A}^{T} \\ \boldsymbol{A} & \mathbf{0} \end{bmatrix} \begin{Bmatrix} \boldsymbol{\varrho}_{GND} \\ \lambda \end{Bmatrix} = \begin{Bmatrix} \mathbf{0} \\ \boldsymbol{\Lambda} \end{Bmatrix}. \tag{2.38}$$

  Therefore, the solution for the GND density in Eq. (2.31) is obtained by simply inverting the coefficient matrix, $\boldsymbol{B}$:

$$[\boldsymbol{B}] = \begin{bmatrix} 2\boldsymbol{I} & \boldsymbol{A}^{T} \\ \boldsymbol{A} & \mathbf{0} \end{bmatrix}^{-1}. \tag{2.39}$$

  This has two conditions for invertibility (Kuhn et al., 1951):

  (1) The stacked matrix $\begin{bmatrix} 2\boldsymbol{I} \\ \boldsymbol{A} \end{bmatrix}$ has linearly independent columns; which is guaranteed given the identity matrix.
  (2) The matrix $\boldsymbol{A}$ has linearly independent rows

  For example, the square coefficient matrix in Eq. (2.38), has a size of $18 + 9 = 27$ for FCC materials, has full-rank and hence can be inverted to find GND densities. The size of the coefficient matrix gets larger as the number of slip systems increases, reducing the computational efficiency, a downside of KKT approach.
- **GND model 1-c:** *Restricted solution to the active slip systems*
  In this model, the total form in Eq. (2.24) is used as the incompatibility measure. The $\boldsymbol{A}$ matrix is reduced to include the GND geometries of only active slip systems, defined with the limit condition on the absolute value of total slip γ^{a}, of (10^{-10} s^{-1}):

$$[\boldsymbol{A}] = \sum_{a} \begin{cases} \varrho_{GND}^{a}\, b^{a}\, \boldsymbol{s}^{a} \otimes \boldsymbol{t}^{a}, & \text{if } |\dot{\gamma}^{a}| > 10^{-10}\ s^{-1}, \\ 0, & \text{otherwise.} \end{cases} \tag{2.40}$$

  Due to the activation of few slip systems, this often results in a rank deficient matrix which requires a generalized pseudo-inverse obtained by SVD. Here, $[\boldsymbol{A}]$ is decomposed into its orthogonal matrices $[\boldsymbol{U}]$, $[\boldsymbol{V}]$, and a diagonal matrix $[\boldsymbol{S}]$:

$$[\boldsymbol{A}] = [\boldsymbol{U}]\, [\boldsymbol{S}]\, [\boldsymbol{V}]^{T}. \tag{2.41}$$

  which is then inverted by taking the transposes of $[\boldsymbol{U}]$, $[\boldsymbol{V}]$ and the reciprocal of the diagonal terms of $\boldsymbol{S}$:

$$[\boldsymbol{A}]^{+} = [\boldsymbol{V}]\, [\boldsymbol{S}]^{-1}\, [\boldsymbol{U}]^{T}. \tag{2.42}$$

  This generalized pseudo-inverse calculates GND densities of the active slip systems only.
- **GND model 1-d:** *Restricted solution to the active slip systems considering configurational changes*
  The incompatibility measure considering configuration changes (Cermelli and Gurtin, 2001) is used in this model as defined in Eq. (2.27). The GNDs are obtained using the same method outlined in GND model 1-c; constraining the solution to the active slip systems followed by SVD and inversion. Therefore, the same relations in Eqs. (2.40) and (2.42) are used to compute the GNDs from incompatibility by eliminating the columns of $\boldsymbol{A}$ of inactive systems.

2.3.4. Rate form (GND model 2)

The rate form of incompatibility uses the curl of a vector instead of using the curl of a second rank tensor which has different forms in the literature (Das et al., 2018). The rate form of the incompatibility is obtained by simply taking the time derivative of Eq. (2.24):

$$\dot{\boldsymbol{\Lambda}} = -\left(\nabla \times \dot{\boldsymbol{F}}_{p}\right)^{T}. \tag{2.43}$$

$\dot{\boldsymbol{F}}_p$ is computed in terms of the plastic velocity gradient, Eq. (2.44):

$$\dot{\boldsymbol{F}}_p = \boldsymbol{L}_p \boldsymbol{F}_p. \tag{2.44}$$

Substituting Eq. (2.2) into Eq. (2.44) gives:

$$\dot{\boldsymbol{F}}_p = \left(\sum_a \dot{\gamma}^a \boldsymbol{s}^a \otimes \boldsymbol{n}^a \right) \boldsymbol{F}_p = \sum_a (\dot{\gamma}^a \boldsymbol{s}^a \otimes \boldsymbol{n}^a) \cdot \boldsymbol{F}_p. \tag{2.45}$$

Substituting Eq. (2.44) into the incompatibility rate in Eq. (2.45) gives:

$$\dot{\boldsymbol{\Lambda}} = -\left\{ \nabla \times \left(\sum_a \boldsymbol{s}^a \otimes \dot{\gamma}^a \boldsymbol{n}^a \cdot \boldsymbol{F}_p \right) \right\}^T. \tag{2.46}$$

Taking the curl into the summation by considering the definition of the curl in Eq. (2.16) gives:

$$\dot{\boldsymbol{\Lambda}} = -\left[\sum_a \left(\nabla \times \dot{\gamma}^a \boldsymbol{n}^a \cdot \boldsymbol{F}_p \right) \otimes \boldsymbol{s}^a \right]^T. \tag{2.47}$$

The incompatibility rate measure per slip system becomes:

$$\dot{\boldsymbol{\Lambda}}^a = -\left[\nabla \times \left(\dot{\gamma}^a \boldsymbol{n}^a \cdot \boldsymbol{F}_p \right) \otimes \boldsymbol{s}^a \right]^T. \tag{2.48}$$

Taking the transpose gives:

$$\dot{\boldsymbol{\Lambda}}^a = -\boldsymbol{s}^a \otimes \left[\nabla \times \left(\dot{\gamma}^a \boldsymbol{n}^a \cdot \boldsymbol{F}_p \right) \right]. \tag{2.49}$$

Using Nye's dislocation tensor for edge and screw dislocations gives the incompatibility as:

$$\dot{\boldsymbol{\Lambda}}^a = b^a \dot{\varrho}^a_{GND,et} \boldsymbol{s}^a \otimes \boldsymbol{t}^a + b^a \dot{\varrho}^a_{GND,en} \boldsymbol{s}^a \otimes \boldsymbol{n}^a + b^a \dot{\varrho}^a_{GND,s} \boldsymbol{s}^a \otimes \boldsymbol{s}^a. \tag{2.50}$$

Equating the incompatibility rate measures in Eq. (2.49) to (2.50) gives Eq. (2.51) in which $\dot{\varrho}^a_{GND,et}$, $\dot{\varrho}^a_{GND,en}$, and $\dot{\varrho}^a_{GND,s}$ stand for GND density evolution rates for edge type dislocations along transverse direction, edge type dislocations along slip plane normal, and screw type dislocations along slip direction, respectively:

$$\begin{aligned} \dot{\boldsymbol{\Lambda}}^a &= -\boldsymbol{s}^a \otimes \nabla \times \dot{\gamma}^a \boldsymbol{n}^a \cdot \boldsymbol{F}_p \\ &= b^a \dot{\varrho}^a_{GND,et} \boldsymbol{s}^a \otimes \boldsymbol{t}^a + b^a \dot{\varrho}^a_{GND,en} \boldsymbol{s}^a \otimes \boldsymbol{n}^a + b^a \dot{\varrho}^a_{GND,s} \boldsymbol{s}^a \otimes \boldsymbol{s}^a. \end{aligned} \tag{2.51}$$

The edge dislocations along the slip normal ($\dot{\varrho}^a_{GND,en}$) are neglected in this study because we assume that edges and screws are restricted to gradients on their glide plane. As the final step, the slip direction vector can be canceled out on both sides of the equations, giving:

$$-\nabla \times \left(\dot{\gamma}^a \boldsymbol{n}^a \cdot \boldsymbol{F}_p \right) = b^a \dot{\varrho}^a_{GND,e} \boldsymbol{t}^a + b^a \dot{\varrho}^a_{GND,s} \boldsymbol{s}^a. \tag{2.52}$$

Equivalently in index notation:

$$-\varepsilon_{ijk} \left(\dot{\gamma}^a n^a_l F_{plk} \right)_{,j} = b^a \dot{\varrho}^a_{GND,e} t^a_i + b^a \dot{\varrho}^a_{GND,s} s^a_i. \tag{2.53}$$

Equations for edge and screw families of dislocations are computed using the vector projections and re-arranging terms giving :

$$\dot{\varrho}^a_{GND,e} = -\frac{1}{b^a} \left(\nabla \times \dot{\gamma}^a \boldsymbol{n}^a \cdot \boldsymbol{F}_p \right) \cdot \boldsymbol{t}^a, \tag{2.54}$$

$$\dot{\varrho}^a_{GND,s} = -\frac{1}{b^a} \left(\nabla \times \dot{\gamma}^a \boldsymbol{n}^a \cdot \boldsymbol{F}_p \right) \cdot \boldsymbol{s}^a. \tag{2.55}$$

The formulations explained here can also be found in Dai (1997). Several different references use the same formulation consistently to quantify GNDs (Busso et al., 2000; Ma et al., 2006).

2.3.5. Slip gradients (GND model 3)

Asssuming small strains ($|\gamma| \ll 1$), the plastic part of the deformation gradient reduces to:

$$\boldsymbol{F}_p = \sum_a \gamma^a \boldsymbol{s}^a \otimes \boldsymbol{n}^a + \boldsymbol{I}. \tag{2.56}$$

Substituting the simplified plastic deformation gradient into Eq. (2.24) and considering the curl of the identity begin equal to zero gives:

$$\boldsymbol{\Lambda} = -\left(\nabla \times \boldsymbol{F}_p \right)^T = -\left(\nabla \times \sum_a \gamma^a \boldsymbol{s}^a \otimes \boldsymbol{n}^a \right)^T. \tag{2.57}$$

The curl operation can be taken inside the sum giving:

$$\boldsymbol{\Lambda} = -\sum_a \left[\nabla \times (\gamma^a \boldsymbol{s}^a \otimes \boldsymbol{n}^a) \right]^T. \tag{2.58}$$

Table 2
Summary of equations used in GND models.

		Incompatibility measure ($\boldsymbol{\Lambda}$)	Coefficient	GND density (ϱ_{GND}) edge ($\varrho_{GND,e}$)	screw ($\varrho_{GND,s}$)
Model 1	a	$-\left(\nabla \times \boldsymbol{F}_p\right)^T$	$\varrho^a_{GND}\, b^a\, \boldsymbol{s}^a \otimes \boldsymbol{l}^a$	$\left[\boldsymbol{A}^+\right]\{\boldsymbol{\Lambda}\}$	
	b	$-\left(\nabla \times \boldsymbol{F}_p\right)^T$	$\begin{bmatrix} 2\boldsymbol{I} & \boldsymbol{A}^T \\ \boldsymbol{A} & \boldsymbol{0} \end{bmatrix}$	$[\boldsymbol{B}]\begin{Bmatrix} \boldsymbol{0} \\ \boldsymbol{\Lambda} \end{Bmatrix}$.	
	c	$-\left(\nabla \times \boldsymbol{F}_p\right)^T$	$\sum_a \begin{cases} \varrho^a_{GND}\, b^a\, \boldsymbol{s}^a \otimes \boldsymbol{l}^a, & \text{if } \lvert\dot{\gamma}^a\rvert > 10^{-10}\ \text{s}^{-1} \\ 0, & \text{otherwise} \end{cases}$	$[\boldsymbol{A}]^+\{\boldsymbol{\Lambda}\}$	
	d	$-\left(\nabla \times \boldsymbol{F}_p\right)^T \boldsymbol{F}_p^T$	$\sum_a \begin{cases} \varrho^a_{GND}\, b^a\, \boldsymbol{s}^a \otimes \boldsymbol{l}^a, & \text{if } \lvert\dot{\gamma}^a\rvert > 10^{-10}\ \text{s}^{-1} \\ 0, & \text{otherwise} \end{cases}$	$[\boldsymbol{A}]^+\{\boldsymbol{\Lambda}'\}$	
Model 2		$-\nabla \times \dot{\gamma}^a\, \boldsymbol{n}^a \cdot \boldsymbol{F}_p$	N/A	$-\frac{1}{b^a}\left(\nabla \times \dot{\gamma}^a\, \boldsymbol{n}^a \cdot \boldsymbol{F}_p\right) \cdot \boldsymbol{t}^a$	$-\frac{1}{b^a}\left(\nabla \times \dot{\gamma}^a\, \boldsymbol{n}^a \cdot \boldsymbol{F}_p\right) \cdot \boldsymbol{s}^a$
Model 3		$\nabla\gamma^a$	N/A	$-\frac{1}{b^a}\boldsymbol{\nabla}\gamma^a \cdot \boldsymbol{s}^a$	$\frac{1}{b^a}\boldsymbol{\nabla}\gamma^a \cdot \boldsymbol{t}^a$

The gradient operation is the sum of the directional derivatives along slip direction, $\boldsymbol{s}^a$, slip plane normal, $\boldsymbol{n}^a$, and line (tangent) direction, $\boldsymbol{t}^a$, Eq. (2.59):

$$\nabla\gamma^a = \gamma^a_{,\boldsymbol{s}^a}\boldsymbol{s}^a + \gamma^a_{,\boldsymbol{n}^a}\boldsymbol{n}^a + \gamma^a_{,\boldsymbol{t}^a}\boldsymbol{t}^a. \tag{2.59}$$

Substituting the directional derivatives and using the definition of curl in Eq. (2.16) to compute the incompatibility gives:

$$\boldsymbol{\Lambda} = -\sum_a \left[\left(\gamma^a_{,\boldsymbol{s}^a}\, \boldsymbol{s}^a \times \boldsymbol{n}^a\right) \otimes \boldsymbol{s}^a + \left(\gamma^a_{,\boldsymbol{n}^a}\, \boldsymbol{n}^a \times \boldsymbol{n}^a\right) \otimes \boldsymbol{s}^a + \left(\gamma^a_{,\boldsymbol{t}^a}\, \boldsymbol{t}^a \times \boldsymbol{n}^a\right) \otimes \boldsymbol{s}^a\right]^T. \tag{2.60}$$

The cross-product of slip plane normals with itself ($\boldsymbol{n}^a \times \boldsymbol{n}^a = \boldsymbol{0}$) is zero which vanishes the effect of slip gradients along the slip plane normal. Substituting $\boldsymbol{t}^a = \boldsymbol{s}^a \times \boldsymbol{n}^a$ reduces Eq. (2.60) to:

$$\boldsymbol{\Lambda} = -\sum_a \left(\gamma^a_{,\boldsymbol{s}^a}\boldsymbol{t}^a \otimes \boldsymbol{s}^a - \gamma^a_{,\boldsymbol{t}^a}\boldsymbol{s}^a \otimes \boldsymbol{s}^a\right)^T = \sum_a \gamma^a_{,\boldsymbol{t}^a}\boldsymbol{s}^a \otimes \boldsymbol{s}^a - \gamma^a_{,\boldsymbol{s}^a}\boldsymbol{s}^a \otimes \boldsymbol{t}^a. \tag{2.61}$$

Equivalently in index notation:

$$\Lambda_{ij} = \sum_a \gamma^a_{,k}\, t^a_k\, s^a_i\, s^a_j - \gamma^a_{,l}\, s^a_l\, s^a_i\, t^a_j. \tag{2.62}$$

Expanding on Eq. (2.24), the dislocation tensor is computed considering the edge and screw families of dislocations using:

$$\boldsymbol{\Lambda} = \sum_a \varrho^a_{GND,e}\, b^a\, \boldsymbol{s}^a \otimes \boldsymbol{t}^a + \varrho^a_{GND,s}\, b^a\, \boldsymbol{s}^a \otimes \boldsymbol{s}^a. \tag{2.63}$$

Therefore, the individual dislocation densities per slip system can be computed by equating the incompatibility to the dislocation tensor:

$$b^a\, \varrho^a_{GND,e} = -\gamma^a_{,\boldsymbol{s}^a} = -\boldsymbol{\nabla}\gamma^a \cdot \boldsymbol{s}^a. \tag{2.64}$$

$$b^a\, \varrho^a_{GND,s} = \gamma^a_{,\boldsymbol{t}^a} = \boldsymbol{\nabla}\gamma^a \cdot \boldsymbol{t}^a. \tag{2.65}$$

The edge dislocation density is the gradient of slip along the slip direction, Eq. (2.66):

$$\varrho^a_{GND,e} = -\frac{1}{b^a}\boldsymbol{\nabla}\gamma^a \cdot \boldsymbol{s}^a. \tag{2.66}$$

The screw dislocation density is the gradient of slip along the transverse direction, Eq. (2.67):

$$\varrho^a_{GND,s} = \frac{1}{b^a}\boldsymbol{\nabla}\gamma^a \cdot \boldsymbol{t}^a. \tag{2.67}$$

2.3.6. Lattice curvature

The lattice curvature is computed using the incompatibility according to Eq. (2.68). This equation ignores elastic strain gradients and computes lattice curvature using total lattice incompatibility obtained by rotations (Arsenlis and Parks, 1999):

$$\boldsymbol{\kappa} = -\boldsymbol{\Lambda}^T + \boldsymbol{I}\ \mathrm{tr}(\boldsymbol{\Lambda})/2 \tag{2.68}$$

2.4. Summary of GND models

Different models relying on the total form (model 1), rate form (model 2), and slip gradients (model 3) are investigated. In addition, four other variants of the total form (model 1) are used to obtain GND densities using; (a) the Least-Squares (L2) minimization (Arsenlis and Parks, 1999), (b) Karush–Kuhn–Tucker (KKT) optimality criterion (Kuhn et al., 1951), (c) restrained

Table 3
Element types and properties.

Abaqus® ID	Geometry	Dim.	Order of GND interpolation	# of nodes per elem. (p)	# of IPs per elem. (q)	condition
CPS4/CPE4	quadrilateral	2D	linear	4	4	p=q
CPS6/CPE6	triangular	2D	quadratic	6	3	p>q
CPS6/CPE6	triangular	2D	linear (CPS3/CPE3)	3	3	p=q
CPS8/CPE8	quadrilateral	2D	quadratic	8	9	p<q
CPS8/CPE8	quadrilateral	2D	linear (CPS4/CPE4)	4	9	p<q
CPS8R/CPE8R	quadrilateral	2D	linear (CPS4/CPE4)	4	4	p=q
C3D8	hexahedral	3D	linear	8	8	p=q
C3D10	tetrahedral	3D	quadratic	10	4	p>q
C3D10	tetrahedral	3D	linear (C3D4)	4	4	p=q
C3D15	prismatic	3D	quadratic	15	9	p>q
C3D15	prismatic	3D	linear (C3D6)	6	9	p<q
C3D20	hexahedral	3D	quadratic	20	27	p<q
C3D20	hexahedral	3D	linear (C3D8)	8	27	p<q
C3D20R	hexahedral	3D	linear (C3D8)	8	8	p=q

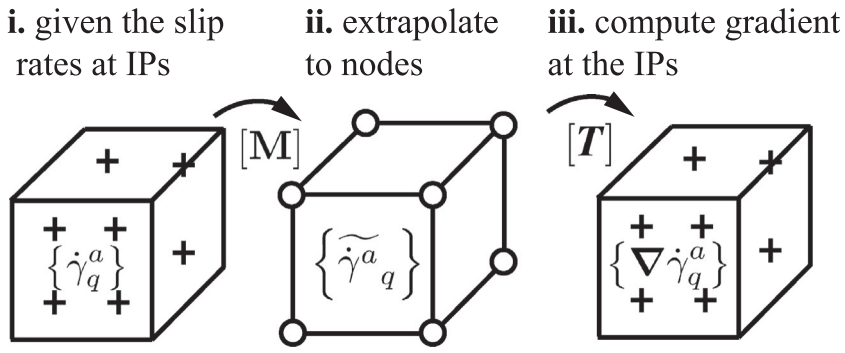

Fig. 3. General gradient calculation procedure shown only for slip gradients. The same procedure applies to the calculation of gradient of $\boldsymbol{F}_p$. Subscript q denotes the integration point at the which the slip rate is computed while the superscript ^{a} denotes the corresponding slip system. The symbol $\tilde{}$ indicates nodal variables.

solution to active slip systems (SS), and (d) incompatibility measure considering deformed areas (Cermelli and Gurtin, 2001) followed by restrained solution to active SS were studied. Table 2 shows the summary of the incompatibility measure, coefficient matrix that needs to be inverted to solve for GNDs, and the expression to compute GND densities corresponding to each model that are used in this study.

2.5. Gradient operator (element type specific)

The gradient operator is computed in the undeformed reference using the initial coordinates once at the beginning of calculations. The gradient calculation is performed by isolating each element from the mesh. This allows calculation of the strain gradients without any special treatment for the grain boundaries. To achieve that, there is only one limiting factor; the number of integration points (IPs), q, must be greater 2 in 2D or 3 in 3D to allow calculation of the directional gradients within the element, respectively.

The gradient calculation was performed with three stages. First, the values of the parameter ($\boldsymbol{F}_p$, $\dot{\gamma}^a \boldsymbol{n}^a \cdot \boldsymbol{F}_p$, or $\dot{\gamma}^a$) at the IPs is obtained. Second, the parameters are extrapolated to the nodes of the element. Third, gradients at the IPs and element center are computed using the gradient operators. Fig. 3 shows these computation steps schematically. The gradient calculation is performed with the shape function gradients in the isoparametric space, $[\boldsymbol{\nabla N}]$, and then transforming the gradient operator to the physical space by Eq. (2.69). $[\boldsymbol{T}]$ is computed at each of the IPs and at the element center.

$$[\boldsymbol{T}]_{(3\times p)} = [\boldsymbol{J}]^{-T}_{(3\times 3)} [\boldsymbol{\nabla N}]_{(3\times p)} . \tag{2.69}$$

The Jacobian is computed using the node coordinates, $\{\boldsymbol{x}\}$, that contains the x, y, z coordinates of each node of an element, Eq. (2.70):

$$[\boldsymbol{J}]^{T}_{(3\times 3)} = [\boldsymbol{\nabla N}]_{(3\times p)} \{\boldsymbol{x}\}_{(p\times 3)} . \tag{2.70}$$

The overall mapping to compute the gradient is given by $[\boldsymbol{G}]$ Eq. (2.71) in which $[\boldsymbol{M}]$ represents the mapping to extrapolate from IPs to nodes:

$$[\boldsymbol{G}]_{(3\times q)} = [\boldsymbol{T}]_{(3\times p)} [\boldsymbol{M}]_{(p\times q)} \tag{2.71}$$

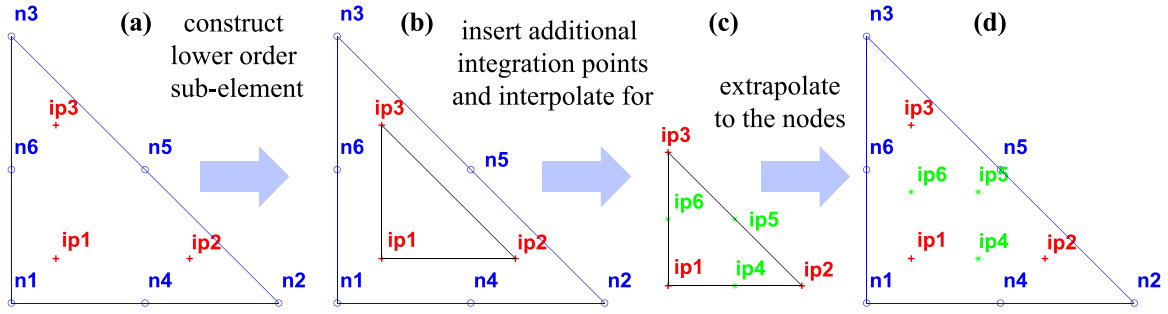

Fig. 4. Extrapolation method for the case $p > q$,e.g. 6-noded quadratic triangle: (a) Element consisting of 6-nodes and 3-integration points, (b) construction of sub-elements, (c) insertion of additional integration points resembling the nodes of the host element, (d) extrapolation from the integration points to the nodes. Example is shown for CPS6/CPE6 types of element for clarity.

The gradients are computed at the integration points and the element centroid. In the case of a homogenized solution, the gradient is computed only at the centroid of the element and the same value of GND density at the element center is assigned to the IPs.

The extrapolation method is different based on the number of IPs (q) and number of nodes (p) of an element which is shown for different types of elements in Table 3. The extrapolation scheme is described for three cases as follows:

2.5.1. Case (p=q)

$[\boldsymbol{N}]$ represents the matrix containing the interpolation functions of each row corresponding to an IP. The inversion in Eq. (2.72) is possible since $[\boldsymbol{N}]$ is a square matrix of full rank without rank deficiency hence is invertable:

$$[\boldsymbol{M}]_{(p\times q)} = \left([\boldsymbol{N}]_{(q\times p)}\right)^{-1}. \tag{2.72}$$

2.5.2. Case (p <q)

If the total number of nodes is less than the total number of IPs, the solution is overdefined hence the inversion of $\boldsymbol{N}$ is possible by calculating the left-pseudo inverse. Therefore the overall inversion mapping that applies to the variables at the IPs becomes:

$$[\boldsymbol{M}]_{(p\times q)} = \left([\boldsymbol{N}]^{T}_{(p\times q)}\,[\boldsymbol{N}]_{(q\times p)}\right)^{-1}[\boldsymbol{N}]^{T}_{(p\times q)}. \tag{2.73}$$

2.5.3. Case (p >q)

In some quadratic elements, the number of nodes per element is greater than the total number of IPs in that element. In this case, direct extrapolation to the nodes is not possible because of the insufficient number of IP in that element. For this reason, $p-q$ additional number of IPs are inserted into the host element. A mapping, $[\boldsymbol{O}]$, is used to interpolate the values at these additional IPs while keeping the existing data at the IPs of the host element using the identity matrix, $[\boldsymbol{I}]$. The mapping is defined in Eq. (2.74) and uses the sub element interpolation functions, $\left[\overline{\boldsymbol{N}}\right]$ which is the shape function of the elements with reduced order (CPS3, CPE3, C3D4, C3D6) of the host element type (CPS6, CPE6, C3D10, C3D15, respectively):

$$[\boldsymbol{O}]_{(p\times q)} = \begin{bmatrix} [\boldsymbol{I}]_{(q\times q)} \\ \left[\overline{\boldsymbol{N}}\right]_{(p-q\times q)} \end{bmatrix}. \tag{2.74}$$

The interpolation mapping $[\boldsymbol{O}]$ is computed by constructing a sub-element, Fig. 4, nodes of which coincide with the integration points of the host element. The position of additional integration points are selected such that the point distribution is the same as the node distribution of the host element.

The total number of nodes of an element and total number of IPs per element becomes equal after the application of the mapping $[\boldsymbol{O}]$, while preserving the existing IP data. The mapping for extrapolation, $[\boldsymbol{M}]$, becomes:

$$[\boldsymbol{M}]_{(p\times q)} = \left([\boldsymbol{N}]_{(p\times p)}\right)^{-1}[\boldsymbol{O}]_{(p\times q)}. \tag{2.75}$$

2.6. Numerical method and important constraints

The crystal plasticity solver details can be found elsewhere (Dunne et al., 2007) in which the residual in the solver is based on Cauchy stress in a user defined subroutine called UMAT. At the end of each time increment non-local GND calculations are performed using the UEXTERNALDB subroutine of Abaqus®. Therefore, GNDs are updated explicitly at the end of each converged time increment. Fortran files, documentation, and examples are available in the GitHub link with open public access (Tarleton, 2023).

Most importantly, a constraint on the increment of the GND density is enforced to avoid accumulation of numerical errors. Slight differences in the slip rates can exist producing artificially large gradients when divided by small numbers at small scales, resulting

Table 4
Model parameters used in the simulations.

C_{11}	C_{12}	C_{44} (G)	b^a	τ_c^0	α	$\dot{\gamma}_0$	n
170 GPa	124 GPa	75 GPa	2.56×10^{-4} μm	1 MPa	0.25	0.001 s^{-1}	20

in low magnitudes of fictitious GND densities. GNDs having a direct effect on CRSS and slip rates amplify those numerical differences further causing a positive feedback. Therefore, a threshold on the increment of the GND density, which corresponds to physically zero dislocation density (2×10^{-10} $\mu m^{-2} = 2\times10^{2}$ m^{-2}) is employed. This threshold is obtained from strain-gradient-free uniaxial tension considering various dimensions which is used to suppress the effect of numerical errors as shown in Eq. (2.76):

$$\varrho^a_{GND} = \varrho^a_{GNDt} + \begin{cases} \Delta\varrho^a_{GND}, & \text{if } \left|\Delta\varrho^a_{GND}\right| > 2\times10^{-10}\ \mu m^{-2} \\ 0, & \text{otherwise} \end{cases} \tag{2.76}$$

3. Results and discussion

The GND calculation procedure was used to simulate FCC single crystals at single slip orientation including a uniaxial tension case without strain gradients, a simple shear case with linear strain gradient, a uniaxial tension case with geometrically imposed strain gradient, and a four-point bending case. In all of the single crystal cases, except the strain-gradient-free case with cube orientation, the crystal orientations were aligned such that only the 1st slip system, $[1\bar{1}0]$ (111), was active. In addition, a polycrystal with fully active slip systems undergoing large deformation was investigated.

In the single crystal cases examined, the deformed area correction (GND model 1-d), gives the same results compared to the case without the area correction (GND model 1-c) because the deformation is in 2D. The 2D plastic deformation does not alter the area normal vector along the third direction (Z-axis), around which the Burger's circuit is constructed. For this reason, model 1-d will only be discussed for the polycrystal case excluding the single crystal single slip cases since it gives the same findings as model 1-c in 2D.

Table 4 shows the material parameters used within this study. The critical resolved shear stress (CRSS), τ_c, was selected as 1 MPa to minimize the effect of elastic deformation. Thermal expansion, creep, and strain hardening due to statistical dislocation interactions were neglected in this study.

3.1. Strain-gradient-free uniaxial tension (single crystal single slip)

Uniaxial tension of a symmetric cube orientation shall reveal zero GND density, $\varrho_{GND} = 0$. To test this case, the cube geometry with unit dimensions in micrometers consisting of eight elements with Euler angles of (°0, °0, °0) was used. The cube orientation was selected intentionally to avoid single slip rotations and to avoid complex stress states. All possible slip systems were active in the analysis without any restriction. The cube was loaded up to a uniform tensile strain of 10% with a strain rate of 0.01 s^{-1}. The opposite face was fixed along the direction of loading (X-axis), allowing contraction in the other two directions normal to loading. The uniaxial loading was simulated in 3D and 2D (plane stress and plane strain) using all of the GND models for all possible element types including; quadrilateral, triangular, hexahedral, tetrahedral, and prismatic element geometries and for both quadratic and linear interpolation functions.

Fig. 5 shows the results for model 1-c and 3D linear solid brick elements. Fig. 5(a) shows the stress–strain behavior with and without (w/o) using the threshold in Eq. (2.76) highlighting the effect of small numerical errors in the exact solution, $\varrho_{GND} = 0$, which accumulate in the gradient calculation, causing a significant difference from an ideally strain-gradient-free case. The error accumulation was no different in case the time increments were 10,000 or 1000, or a free time stepping was used, suggesting that the source of the error was not the time integration. Similarly, decreasing the convergence tolerances on both the equilibrium solver of Abaqus® and crystal plasticity solver three orders of magnitude from their initial value made no difference in the results. These findings suggest that artificial gradients arise independent of the equilibrium and crystal plasticity solvers. Only the threshold on GND increment could avoid formation of this artifact which corresponds to a no strain gradient hardening case as the expected behavior for a strain gradient-free uniaxial tensile test. Fig. 5(b) and (c) show the comparison of GND density on an active slip system at the end of loading (10% strain) with and without (w/o) using the threshold, respectively.

The procedure was repeated for a larger sample with millimeter dimensions. In this case, these artificial gradients were still present but with relatively low magnitudes causing no strain hardening which validates the size dependence of the artifact. Small differences in the slip rates between the integration points were still present giving rise to small but nonzero amounts of GND density. These small differences amplify over small micrometer dimensions leading to non-negligible values of GND density.

The results were exactly the same for all elements and models except in the plane strain case where the von Mises stress was 2.41 MPa compared to the plane stress case due to higher constraint in plane strain conditions. This discrepancy arises because the plane strain formulation was designed to restrict displacement in the normal to loading direction in 2D (Z-axis). As a result, the use the threshold on the GND increment leads to consistent results regardless of the element type used.

The threshold of 2×10^{-10} μm^{-2} was computed by trial and error. The selected threshold was tested and validated for a range of externally applied strain rates of 0.1 s^{-1}, 0.01 s^{-1}, and 0.001 s^{-1} and also for a range of rate sensitivity exponents, n in Eq. (2.12), with values ranging of 0.1, 10, and 100.

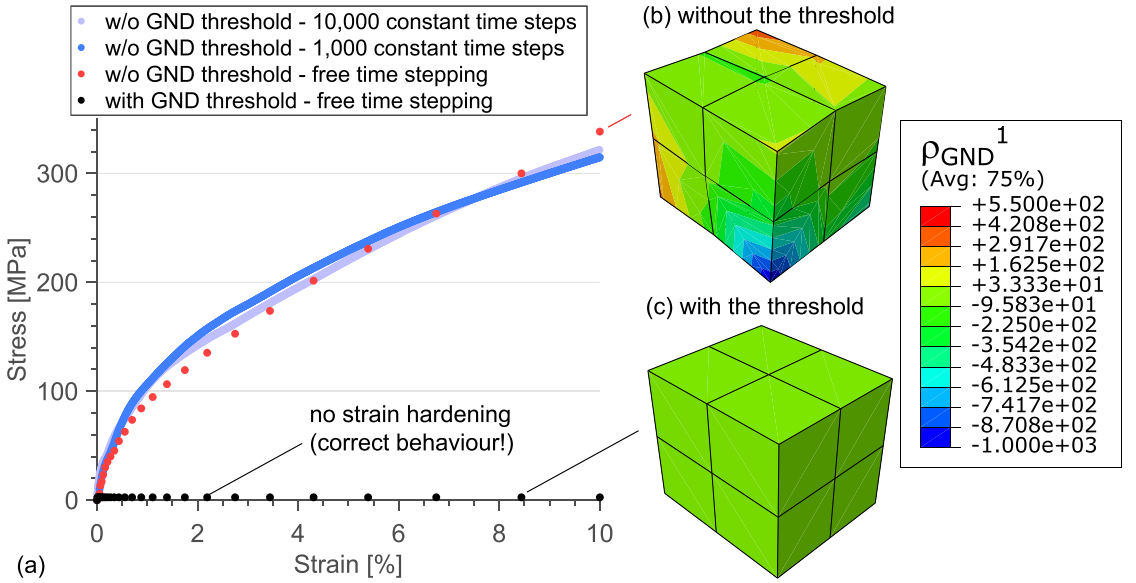

Fig. 5. (a) Average of the axial stress over the integration points, (b) GND density on slip system - 1 without the threshold, and (c) GND density on slip system - 1 with the threshold. A uniaxial tensile strain of 10% with a strain rate of 0.01 s^{-1} was used. No strain gradient hardening is expected for a uniaxial tension load indicated with the black dots.

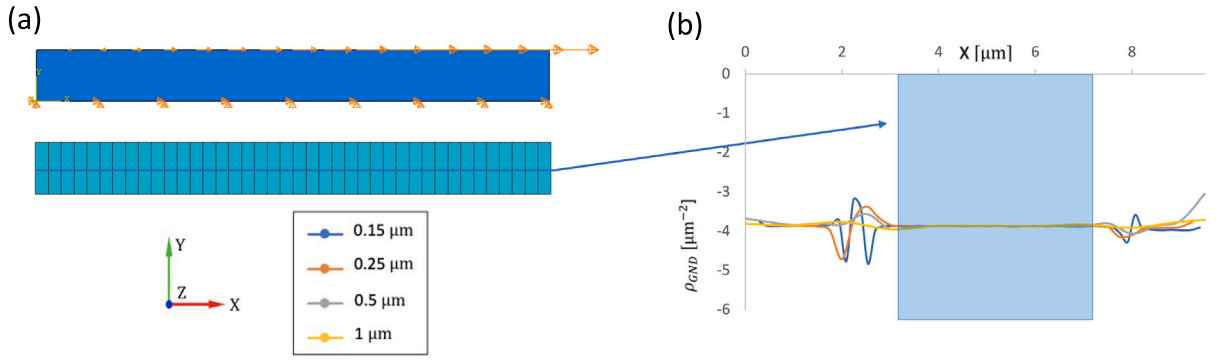

Fig. 6. (a) Boundary conditions and mesh of strip of elements, (b) GND density distribution in the middle nodes for different mesh sizes of 1, 0.5, 0.25 and 0.15 μm and using GND model 1-c.

3.2. Simple shear of a strip

A strip of elements with a height and length of 1 μm and 10 μm, respectively, was used with a strain gradient applied by linearly varying shear displacements applied on the top edge of the strip. It should be noted that, in the presence of a shear gradient, a normal strain/stress component along the shear direction arises as a result of equilibrium which deviates from a simple shear case to a complex deformation. The shear displacement on the strip was linearly proportional to the position along X-direction, Fig. 6(a), which gradually increases up to 10^{-2} μm at the top right corner and was applied over a time duration of 1 s which corresponds to a maximum strain of 1% and a strain rate of 10^{-2} s^{-1}. The analytical value of the GND density for this case was calculated dividing the applied shear strain by the length of the strip and by Burgers vector; 10^{-2} μm / (10 μm × 2.56×10^{-4} μm) = −3.9 μm^{-2}. The edge dislocation density with a negative sign was obtained for a positive shear gradient along the slip direction, which was as expected (Arsenlis and Parks, 1999). Bunge angles to facilitate single slip were (−135, 35.2, 180) with a CRSS of 1 MPa and the remaining slip systems were deactivated imposing a high value for CRSS (10^6 MPa). Both plane stress (CPS8) and plane strain (CPE8) elements were investigated.

3.2.1. Mesh convergence

To conduct a rigorous convergence analysis, the GND density values were measured in the CPS8 elements for different mesh sizes. The density was plotted along the length of the strip (X-direction in Fig. 6(a)) using model 1-c for GND calculations.

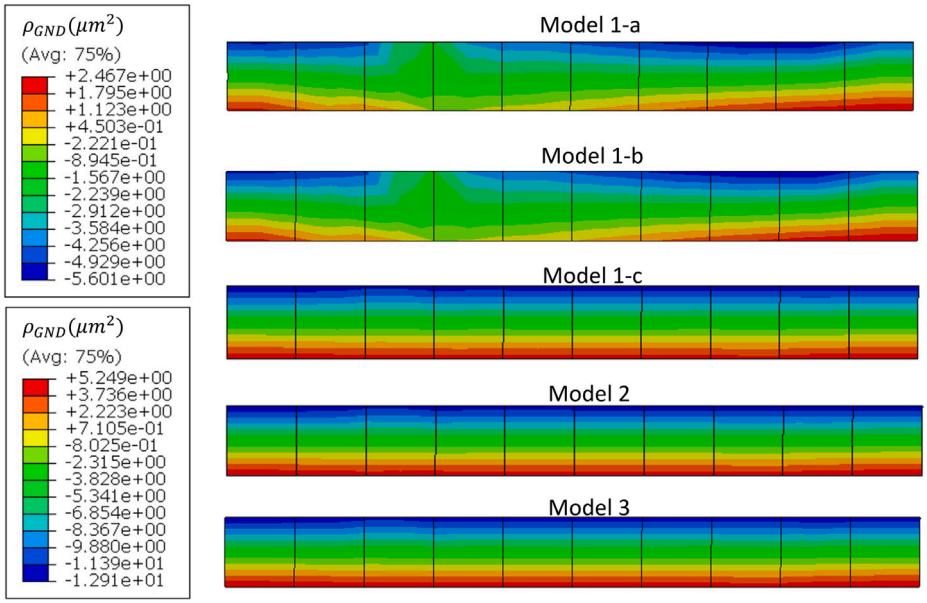

Fig. 7. Average values of GND density for different GNDs models of the strip under a shear gradient for quadratic plane stress elements (CPS8): model 1-a, model 1-b, model 1-c, model 2, and model 3 after shear strain of ~1% with a strain rate of 10^{-2} s^{-1}. The analytical solution is $\varrho_{GND} = -\frac{1}{b}\nabla\gamma \cdot \boldsymbol{s} = -3.9$ μm^{-2}.

Fig. 6(b) show the convergence of GND density at the center nodes of the strip for different mesh sizes. However, the fluctuations were present at the two ends of the strip due to excessive shear distortions in the first and last elements. The GND density at the center of the element was approximately the same in all the simulations with an average magnitude of -3.85 μm^{-2}, which is in excellent agreement with the analytical GND density of -3.9 μm^{-2}.

3.2.2. GND model

Different GND models were compared using the same element type and for a converged mesh. Quadratic quadrilateral plane stress elements (C3PS8) with a mesh size of 1 μm were used. Fig. 7 shows the GND density in the active slip system. The GNDs on the remaining slip systems vanished for models 1-c, 2 and 3 while nonzero GND values were computed for models 1-a and 1-b for the inactive slip systems. Therefore, models 1-a and 1-b reveal nonphysical GND densities on inactive slip systems by either L2 minimization (model 1-a) or KKT optimization (model 1-b). Therefore, the restriction of the solution of GND densities to the active slip systems, as for model 1-c, is essential to obtain physically relevant results.

The analytical solution for the GND density reveals: $\varrho_{GND} = -\frac{1}{b}\nabla\gamma \cdot \boldsymbol{s} = -3.9$ μm^{-2}. The results produced by GND models 1-a and 1-b show the same GND distribution, which is typical for the shear strain gradient, except for some elements. The GND density of the models 1-a and 1-b in the middle of the elements was approximately constant having a value of -1.94 μm^{-2}. GND models 1-c, 2, and 3 exhibited a constant GND distribution with -3.85 μm^{-2}. Those were in excellent agreement with the analytical solution than that of the models 1-a and 1-b.

3.3. Uniaxial tension with strain gradient

A strain gradient without varying the externally applied load or displacement spatially is also possible by using a gradient geometry. To achieve that, Kuroda (2011) used a uniaxial load that was applied to a material with two slip systems in a double slip configuration. As a result of the varying cross section in the sample geometry, two slip bands formed in a cross shape with decreasing slip intensity as a function of the width of the sample thereby leading to the generation of strain gradients and GNDs.

Fig. 8(a) shows the geometry of the model used in this analysis. The tensile force along the Y-axis is uniform. However, varying the area, A, leads to a variation in stress along the Y-direction that results in a stress/strain gradient. The strain gradient varies approximately according to: $\frac{F}{A} = \sigma = E\varepsilon \rightarrow \frac{-F}{EA^2}\frac{dA}{dy} = \frac{d}{dy}\left(\frac{F}{EA}\right) = \frac{d\varepsilon}{dy}$.

The cross section area in the test sample was calculated as a function of position at the Y-axis according to: $A = (-2\sqrt{R^2 - y^2} + 2R + a)\,d$ where $y = 0$ was the narrowest location in the cross section, $R = 12.5$ μm was the radius of curvature of the edges at the sides, $a = 5$ μm was the minimum value of the width, $A = 10$ μm was the maximum value of the width at $y = \pm 7.5$ μm, $d = 1$ μm was the thickness along the Z-axis, and $L = 25$ μmm was the total length.

The total vertical displacement of 0.01 μm was applied in 1 s loading time corresponding to a total strain and strain rate of 0.5% and 0.005 s^{-1}, respectively. The opposite face was fixed in the Y direction and one of the corners was fixed in the X direction to prevent lateral displacement of the sample.

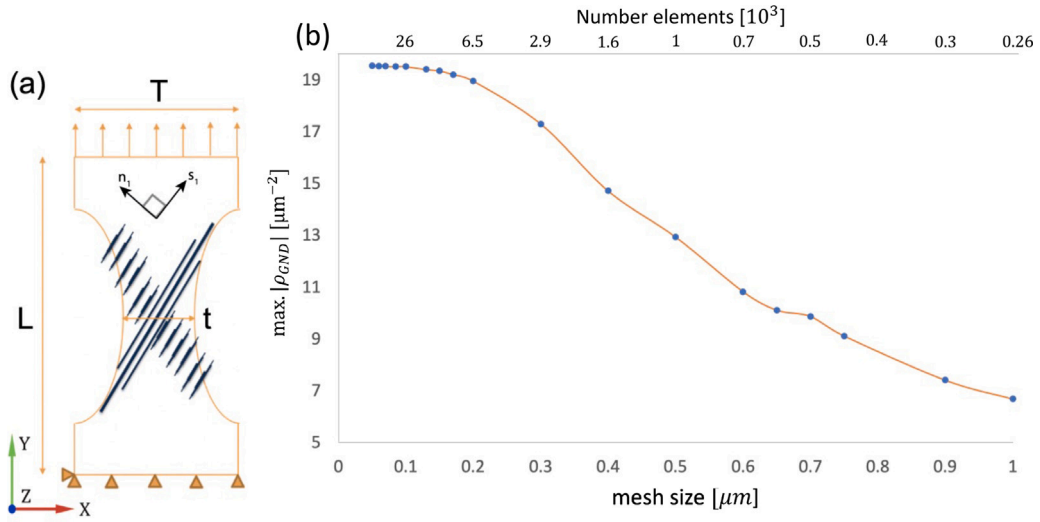

Fig. 8. Uniaxial tension with a strain gradient sample geometry for quadratic plane stress elements (CPS8) (a) sample geometry and boundary conditions and (b) GND density convergence with mesh refinement.

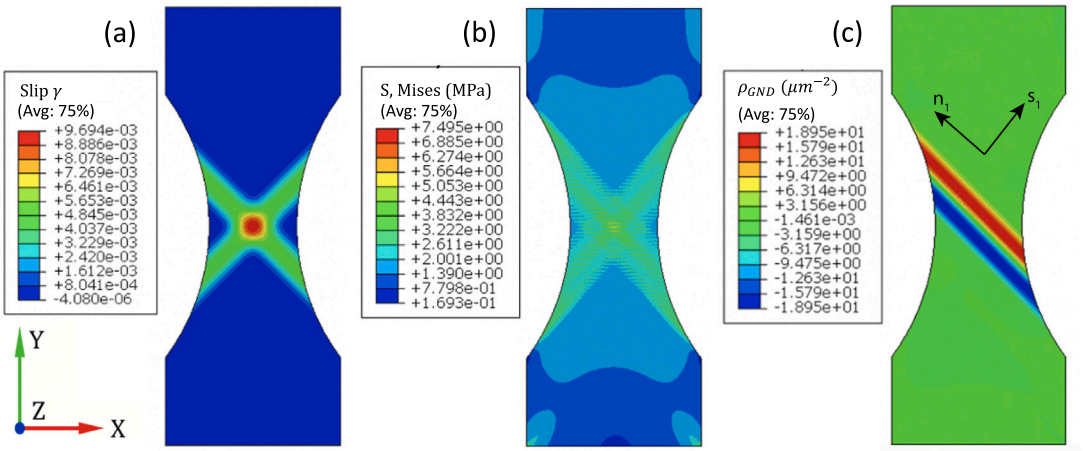

Fig. 9. Distributions of (a) total slip, (b) von Mises stress, (c) GND density on the active slip system after uniaxial tensile strain of 0.5% with a strain rate of 0.005 s^{-1} using model 1-c.

The slip system $\langle 1\bar{1}0 \rangle$ {111} was oriented with a 45° angle with respect to the loading axis (Y direction) to facilitate single slip, Fig. 8(a), thereby giving Bunge angles of (–135, 35.2, -135). The active slip system had a CRSS of 1 MPa while the remaining slip systems were deactivated by imposing a CRSS of 10^6 MPa. Plane stress quadratic quadrilateral elements (CPS8) were used.

3.3.1. Mesh convergence

The convergence study was conducted in the 2D model using model 1-c. Fig. 8(b) represents the maximum value of the GND density obtained based on the mesh size. The maximum GND density was used as the measure for the convergence because it occurred at the center of the sample and it was consistently the same for both positive and negative GND bands.

GND density remains unchanged after the mesh size was reduced to 0.2 μm, with a maximum value differing below 1% that of the finer mesh (0.05 μm), Fig. 8(b). Therefore, a mesh size of 0.2 μm was selected as the converged mesh and used for the simulations using models 1-c, 2 and 3. However, convergence was not achieved for models 1-a and 1-b for this mesh size. Therefore, the mesh size was 0.5 μm^2 for models 1-a and 1-b to give converged results.

3.3.2. Results

Fig. 9(a) and (b), show the deformation in the form of a shear band with a cross shape, although only a single slip system was active contrary to Kuroda (2011). This is because the Schmid tensor does not differentiate between the slip direction and slip plane normal, therefore there is no distinction between a slip band and a kink band Marano et al. (2019). For small deformations, the total

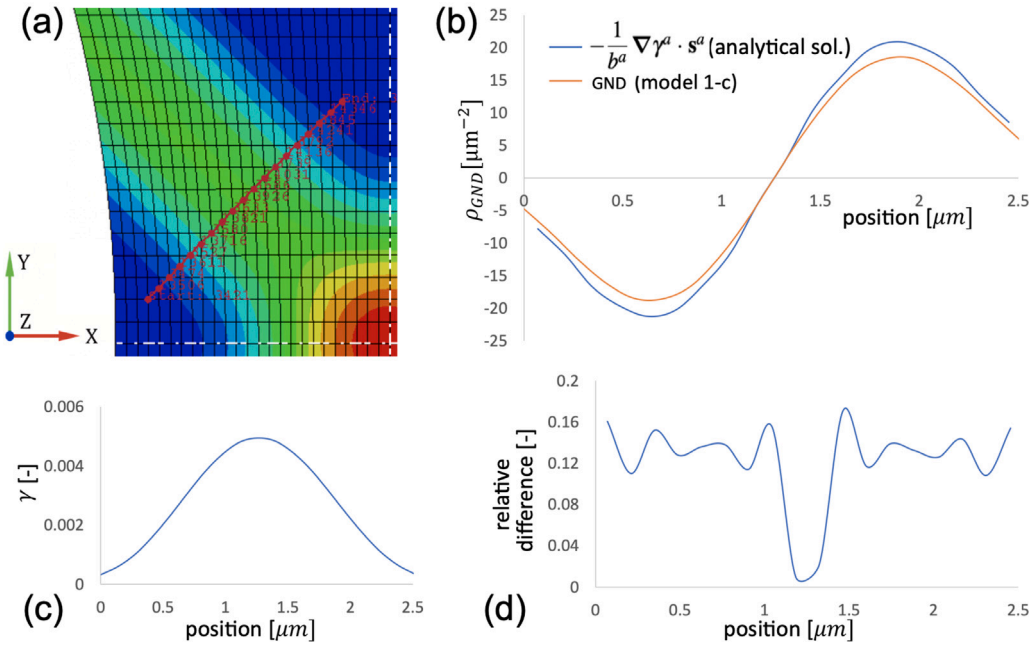

Fig. 10. (a) Path across the slip band for the GND plots (color scale is the same as in Fig. 9(a)), (b) GND density profile, (c) slip profile along the path, and (d) relative error between the theory and model 1-c.

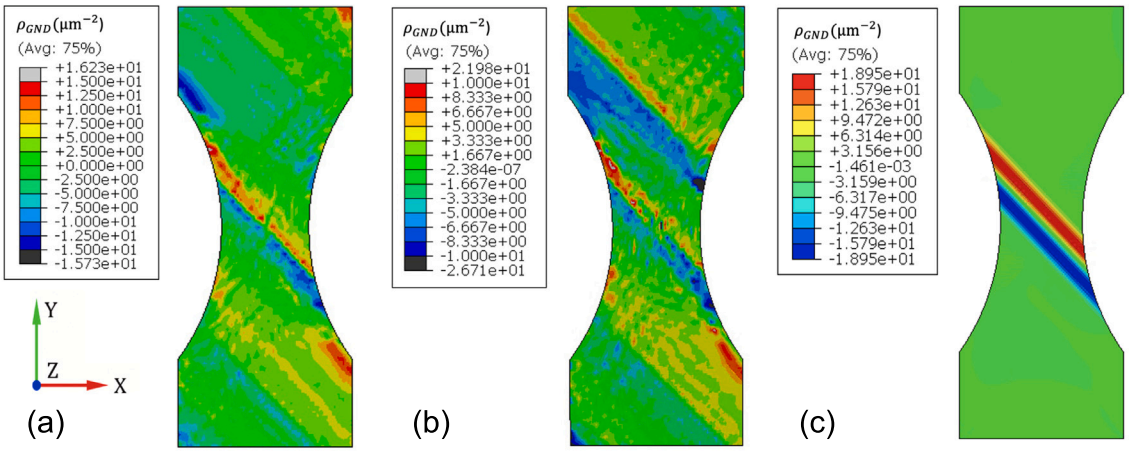

Fig. 11. GND profile for (a) model 1-a, (b) model 1-b, (c) model 1-c after uniaxial tensile strain of 0.5% with a strain rate of 0.005 s^{-1}. The results when using linear elements as well as model 2 and model 3 are very similar to the results of the model 1-c, hence not included due to space limitations.

slip, γ, remains symmetric. On the other hand, as the strain increases (~3% of strain), the kinematic constraints and the increase in the GND density leads to loss of the symmetry of total slip.

The distribution of von Mises stress was similar to strain or slip, Fig. 9(b). The stress concentrations at the end corners were also present but smaller than the CRSS, τ_c, which were not high enough to activate slip.

Fig. 9(c) shows the GND density obtained by model 1-c, with two equal bands of positive and negative GND along one of the diagonals of the slip band with cross-shaped. The amount of slip, γ, was similar in both diagonals, but the orientation of the slip gradient was different. Fig. 8(a) shows a schematic illustration of the slip distributions. The stress in the center of the specimen is highest due to the gradient geometry. The distribution of the slip was determined on the basis of the direction of the active slip system, s^1 and the stress.

The density of the edge dislocations was calculated analytically using the amount of slip over a path parallel to the slip direction, Fig. 10(a). The slip gradients ($\varrho^a_{GND} = -\frac{1}{b^a}\nabla\gamma^a \cdot s^a$) were used for the analytical calculation. Fig. 10(b) shows the quantity of GND

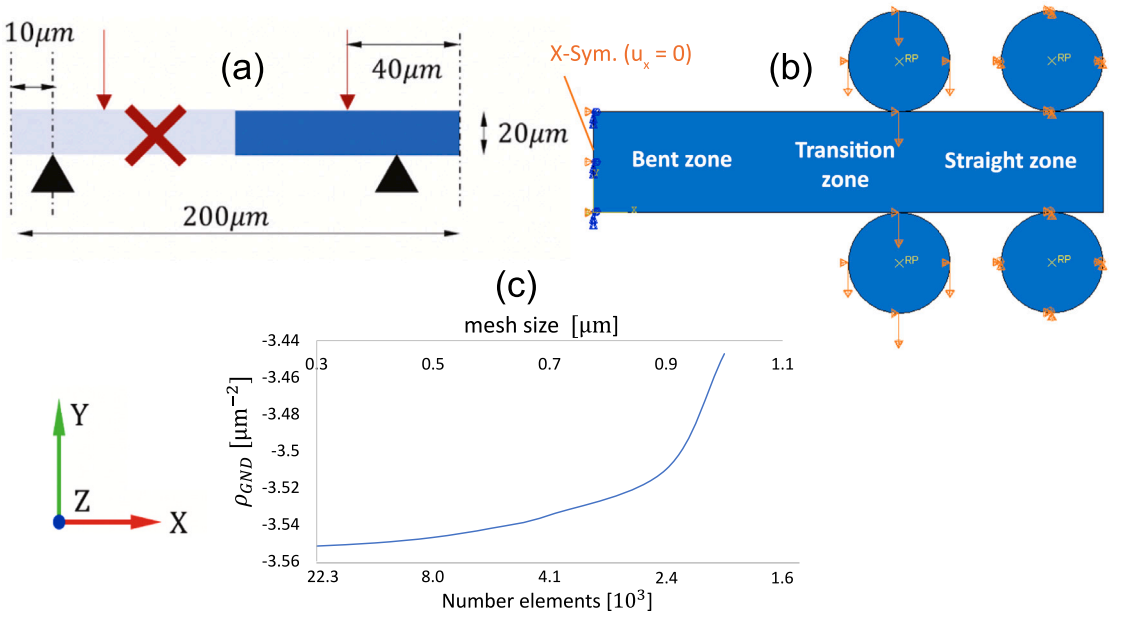

Fig. 12. Four-point bending (a) beam dimensions and symmetry (the red cross sign indicates the neglected portion of the beam using symmetry), (b) boundary conditions based on Xu (2021b), and (c) mesh convergence.

density to compare the analytical solution and that of model 1-c which was shown in Fig. 10(c). The relative difference between the analytical solution and GND model 1-c did not exceed 17%, as illustrated in Fig. 10(d).

Fig. 11 shows a comparison of GND density distributions obtained by the three variants of total form, models 1-a, 1-b, and 1-c. GND models 1-a and 1-b exhibit a distribution of GNDs forming positive and negative bands in the center of the sample and at the end points of the curved edges, Fig. 11(a)–(b). Both models reveal a reasonable profile in the center of the piece in the presence of two bands. However, GND densities in slip systems other than the active ones cast doubt on the results of GND models 1-a and 1-b. In addition, according to the analytical model, narrowing down the cross section should produce strain gradients at the center of the structure instead of at the base where no GND density was expected.

GND model 1-c using both linear and quadratic interpolation functions, model 2, and model 3 revealed the same result illustrated in Fig. 11(c), showing the two dislocation bands and slip band with a cross shape. The simulation times for the mesh with 6500 CPS8 type elements (with a mesh size of 0.2 μm) were compared . Models 1-a and 1-b exhibited computation times that are approximately eight times greater than the rest of the models. This was attributed to the L2 method that reveals GNDs in inactive slip systems causing excessive strain hardening on the primary system. Therefore, models 1-a and 1-b exhibited poor convergence behavior.

3.4. Four-point bending

The four-point bending case has been extensively used to investigate the size dependence based on strain gradients because the strain gradient within the beam can be well established in the form of a linear variation toward the neutral axis, which implies a constant density of GND (Li and Fang, 2020; Erinosho and Dunne, 2014). The finite element model shown schematically in Fig. 12 is similar to Xu (2021b). The half-beam dimensions of length, thickness and width were 200 μm, 20 μm, and 2 μm, respectively. The beam was supported and displacement loaded by rigid solid bodies (circles or cylinders) at distances of 10 μm and 40 μm from the free end, respectively. Using the symmetry axis normal to the X-axis on the left-end of the beam ($u_x = 0$), half of the beam was simulated. The beam displacements were applied over 20 s time intervals, giving a total bending strain of 0.75% and a strain rate of 3.75×10^{-4} s^{-1} for positive/negative bending and straightening. Bunge angles were (−135, 35.2, −135) with respect to the X–Y–Z axis shown in Fig. 12 such that the slip system $\langle 1\bar{1}0 \rangle \{111\}$ makes 45° with the neutral axis of the beam and the slip plane normal was perpendicular to the width axis of the beam (Z-axis in Fig. 12(a)), thus a single slip can be facilitated. The active slip system had a CRSS of 1 MPa, and the remaining slip systems were deactivated by imposing a CRSS of 10^6 MPa.

Four-point bending was achieved using rigid bodies with a radius of 10 μm. The deformation was induced through three stages to investigate GND formations after positive bending and straightening, followed by negative bending.

As explained previously, GND formation can be positive or negative; the notation used in all the models was based on Arsenlis and Parks (1999), Xu (2021b) which defines the slip gradient along the slip direction as a negative edge type GND.

In the *positive bending* stage, end displacement of $u_y = -1$ μm was applied in the Y-direction using the rigid body located at the top left in Fig. 12(b), while the rigid bodies on the right were fixed. A displacement of $u_y = -1.1$ μm in the Y-direction was applied on the rigid body at the bottom left to prevent contact with the beam.

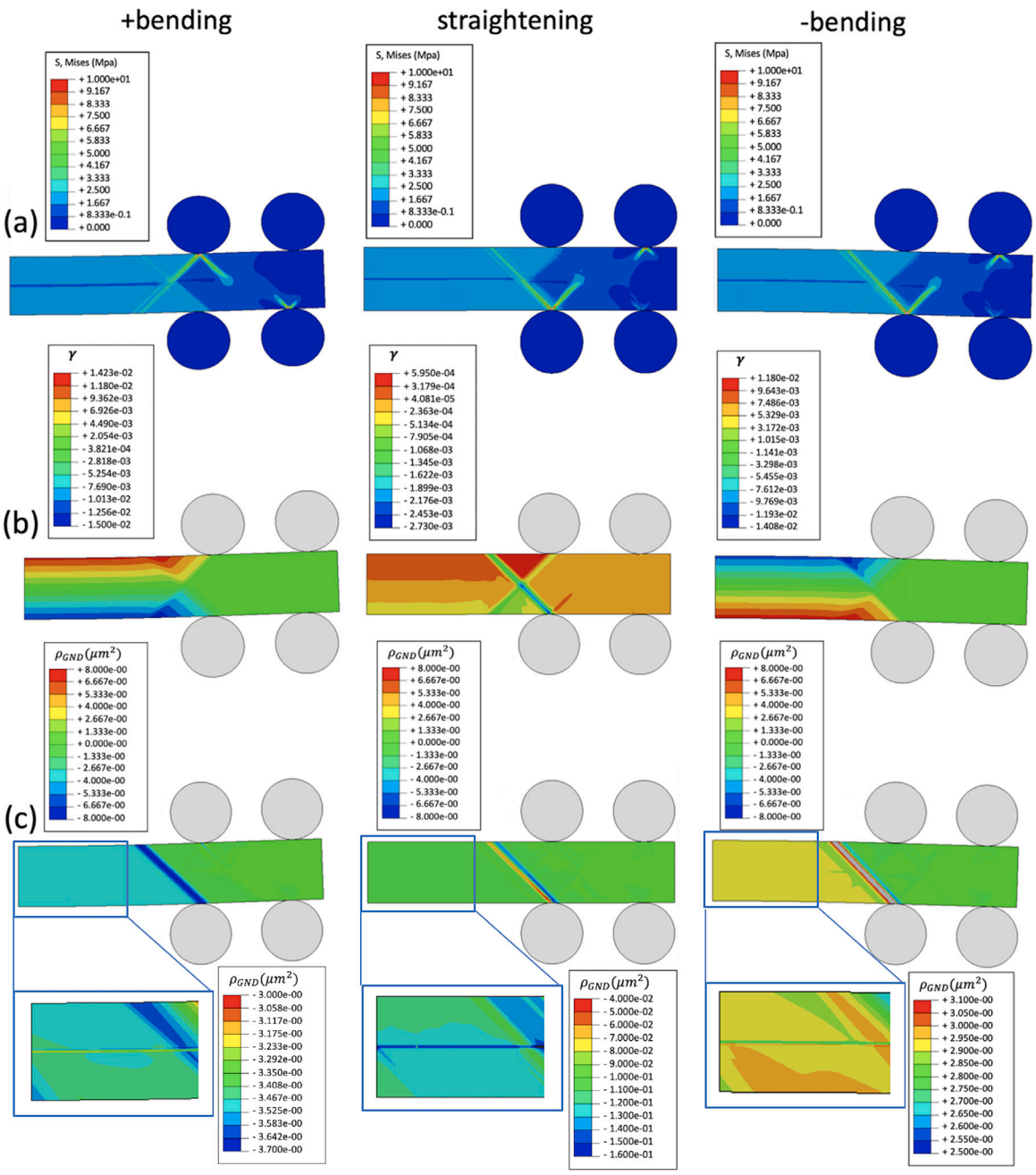

Fig. 13. (a) von Mises stress, (b) total slip γ, and (c) ϱ_{GND} after positive bending (leftmost column), straightening (mid-column), and negative bending (rightmost column) with a bending strain of 0.75%, strain rate of 3.75×10^{-4} s^{-1} and using model 1-c.

In the *straightening* stage, the direction of the load was reversed. The rigid body at the bottom left moves with $u_y = 1.1$ μm when straightening the beam, while the rigid body at the top left moves with $u_y = 1.2$ μm, disengaging from the beam.

In the *negative bending* stage, the rigid bodies on the left side displace an additional $u_y = 1$ μm compared to straightening, causing the beam to bend in the opposite direction. The rigid bodies on the right remained fixed along both X and Y directions throughout the deformation.

3.4.1. Mesh convergence

The convergence study in 2D was conducted for quadratic quadrilateral plane stress elements (CPS8). In this case, the maximum value of GND density was not taken into account (as was the case in the convergence study of uniaxial strain gradient) because this

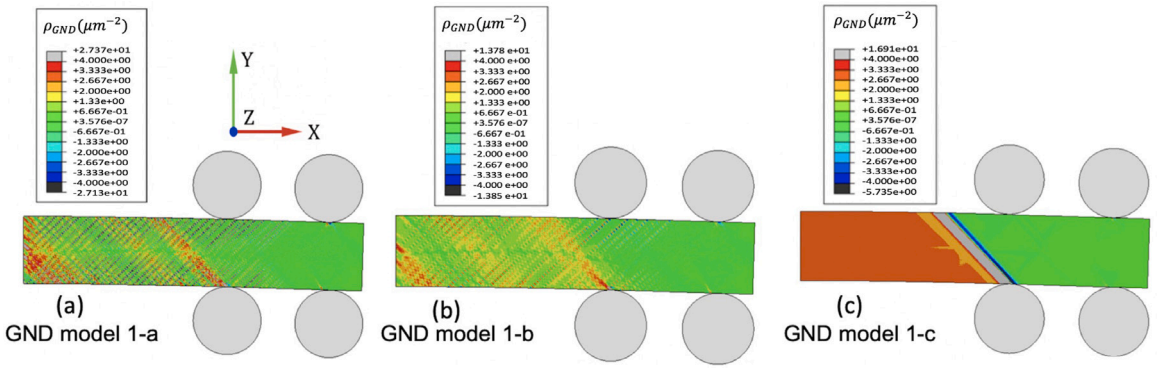

Fig. 14. GND density after negative bending for different GND models: (a) model 1-a, (b) model 1-b, and (c) model 1-c for a bending strain of 0.75%, strain rate of 3.75×10^{-4} s^{-1}.

value occurred at the contact point between the rigid bodies and the beam that is outside of the bent zone. Therefore, the average value of the GND density on the left face of the beam (in the bent zone) was used as the convergence measure.

Fig. 12(c) shows the average value of the GND densities that were obtained after positive bending, as a function of the element size using model 1-c. The results had approximately 3% difference from each other. Therefore, the mesh size was selected as 0.5 μm for the four-point bending simulations.

3.4.2. Results

The beam was divided into three different zones based on the main characteristics of the deformation, Fig. 12(b) similar to the experimental and simulation findings in Erinosho and Dunne (2014). The bent zone is the region of greatest interest in four-point bending tests. The straight zone is in between the rigid bodies and it does not significantly bend; as a consequence, no significant GNDs were produced with the exception of the contact regions with the rigid bodies. The transition zone exhibits the highest strain gradients and hence the highest GND densities.

Fig. 13 shows an overview of von Mises stress, total slip, and GND density distributions calculated using model 1-c for a 2D simulation with 8000 quadratic quadrilateral (CPS8) elements.

After positive bending, the von Mises stress distributions in the bent zone was consistent while local stress concentrations were present at the upper-left and lower-right rigid body contact locations. The slip profile was similar to the one described in the literature (Xu, 2021b), with the bent zone being particularly important as the slip increases steadily from bottom to top. This results in a nearly constant GND density in the bent zone that ranges from -3 μm^{-2} to -3.7 μm^{-2}, the highest variations occur close to the transition zone and in the neutral axis where there is a discontinuity in the GND profile. The discontinuity arises from the non-slip condition on the neutral axis, while the slip gradient was present due to bending. In the transition zone, a band of negative GNDs with a density of ~ -8.06 μm^{-2} was observed, which was related to the change in curvature between the bent and straight zones, where the GND density almost vanished because there was no strain gradient.

After the straightening, the calculation of the GND density becomes approximately zero, which indicates recombination of negative GNDs with the accumulating positive GNDs upon straightening. A stress profile similar to the positive bending was observed, with the highest concentrations of stress present at the contact locations of the rigid bodies with the beam, specifically the lower-left and upper-right rigid bodies. The presence of residual stress was observed in the contact region of the lower-right rigid body, which was no longer in contact with the beam. Again, the amount of slip was reduced by several orders of magnitude, approaching nearly zero after straightening. Similarly, the GND density in the bent zone had values ranging from -0.04 μm^{-2} to -0.16 μm^{-2}, the lowest value being on the neutral axis (a region particularly difficult to calculate due to non-slip condition). However, in the transition zone, the band of negative GNDs did not completely dissapear. Instead, a parallel band of positive GNDs was generated with a density of 7 μm^{-2} adjacent to the negative band.

After the negative bending, a positive GND density in the bent zone was expected. The von Mises stress distribution remained similar to that after straightening. The slip profile was also quite similar to that after positive bending, but with the sign reversed. In the transition zone, the negative band of the GNDs was reduced to approximately -5 μm^{-2}, while the positive band increased to almost 15 μm^{-2}. The GND density in the bent zone ranges from 2.5 μm^2 to 3.1 μm^2. Negative GNDs disappear when the curvature changes. However, in regions where the deformation was higher (such as the transition zone or the contact zone with the rigid bodies), some negative GNDs persist after negative bending.

3.4.3. GND model (2D)

Fig. 14 shows the comparison of different GND models after negative bending. GND models 1-a and 1-b reveal similar findings; the GND bands were observed along the slip direction and slip plane normal. The bands in the direction of slip contain both positive and negative GND densities with higher values in the regions with pronounced slip, γ. This was due to the influence of numerical noise in the model, similar to the case of a uniaxial strain gradient, and the noise was associated with the method used to solve for

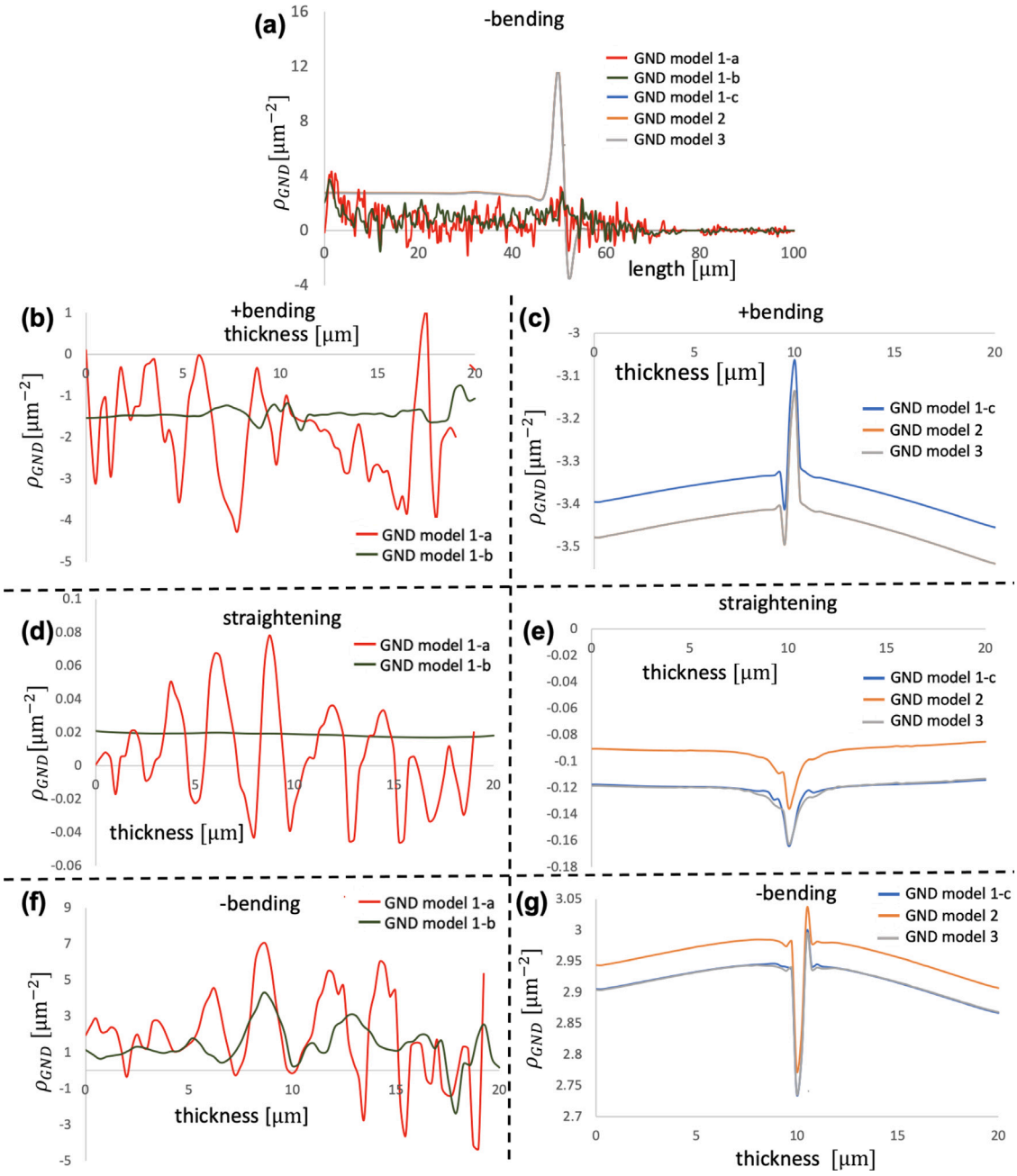

Fig. 15. GND density vs. (a) length after negative bending for all of the models, (b) thickness for models 1-a and 1-b after positive bending, (c) thickness for models 1-c, 2 and 3 after positive bending, (e) thickness for models 1-a and 1-b after straightening, (f) thickness for models 1-c, 2 and 3 after straightening, (g) thickness for models 1-a and 1-b after negative bending, (h) thickness for models 1-c, 2 and 3 after negative bending. All model findings are not shown on the same plot for clarity.

GNDs. The bands in the normal direction exhibit positive GND densities, as expected considering the sign of the curvature. There were high GND densities at the end of the beam where the curvature was greatest, as well as along the band that was located between the two leftmost rigid bodies, which is consistent with the other models.

The main issue in models 1-a and 1-b is linked with the occurrence of GND densities on the inactive slip systems which are not physically representative. The computed densities were lower but still significant, accounting for approximately 20%–30% of the GND densities in the active slip systems.

Models 1-c, 2, and 3 give the same 2D GND profile similar to the uniaxial tension case. Path plots of the GND density along the thickness directions (Y-axis) and length directions (X-axis) were included for more detailed comparison. The findings for models 1-a and 1-b are shown separately in Figs. 15(b)–(d)–(f) due to noise resulted in these models for clarity.

In Fig. 15(a), the horizontal path after the negative bending shows a density of positive GND density in all models (consistent with the curvature). Models 1-a and 1-b exhibited a density profile with oscillations, with the maximum GND density value located at the left face of the beam, which gradually decreases towards the zone between the rigid bodies where the beam possesses no curvature. In the transition zone, there was a second peak of positive GND density followed by a decrease until the value reached zero. In models 1-c, 2, and 3, a constant GND density was computed throughout the bent zone until it reached the straight zone. The transition zones posses two bands with high density of positive and negative GNDs, while the straight zone had zero GND density.

GND density changed its sign to negative values after positive bending as expected, Fig. 15(b) and (c). Model 1-a exhibited a large number of oscillations, even reaching positive values ($1\ \mu m^{-2}$ at thickness position of $17\ \mu m$). The GND density obtained from model 1-a differs by 48% with respect to that of models 1-c, 2, and 3. Model 1-b was more consistent, which is in agreement with the four-point bending theory, but it still differs by 61% from model 3. In contrast, models 1-c, 2, and 3 show almost constant GND density values that are in perfect agreement with the analytical solution ($-3.4\ \mu m^{-2}$) within the bent zone. The largest difference was 10% from the average value and occurred at the central axis of the beam where the amount of slip, γ, changed its sign, suggesting a possible distortion in the elements in that region. The remaining findings were very similar revealing a difference in the GND density less than 2%.

Fig. 15(d) and (e) show GND density variations along the thickness direction after the straightening. Model 1-a exhibited positive and negative oscillations, while model 1-b shows a constant profile, both profiles nearly zero densities. However, models 1-c, 2, and 3 exhibited a low residual constant density of approximately $-0.1\ \mu m^{-2}$.

Fig. 15(f) and (g) show GND densities along the thickness direction after negative bending. Model 1-b revealed an inhomogeneous profile, while it became quite homogeneous after negative bending (Fig. 15(b)) and after straightening (Fig. 15(d)). This behavior was attributed to high sensitivity to initial conditions (pre-existing GND). The average difference with respect to the model 3 is 44% for model 1-a and 62% for model 1-b. However, models 1-c, 2, and 3 exhibited almost the same constant value of $2.9\ \mu m^{-2}$ which was slightly different from the analytical value of $3.4\ \mu m^{-2}$. The analytical value of the GND density was computed on the basis of the slip gradients. GND density annihilates upon load reversal while leaving a certain amount of residual strain and the GND density.

3.4.4. Comparison of 2D and 3D models

A 3D finite element model consisting of 32,000 quadratic hexahedral elements (C3D20) was used to provide a comparison to the plane stress simulations. The GND distributions were similar for 2D and 3D, being nearly homogeneous along the Z-axis, highlighting a good match between 2D and 3D models, Fig. 16. However, higher stresses were observed in 3D at the contact zone between the rigid bodies and the bar, and a band of positive and negative GNDs appears in the upper-right corner of the bar. This is related to both the upper and lower rigid bodies that must remain in contact constantly with the specimen to prevent displacements along the Z-axis after positive bending, straightening, and negative bending.

The bent zone had almost identical GND densities in both the 2D and 3D models. The difference was greater near the rigid bodies. For example, the negative GNDs after positive bending remain during straightening for the 2D model. However, these differences have minimal impact on the bent zone.

Fig. 17 shows the GND density along the thickness direction on the left face of the beam after negative bending for the 3D case, including different GND models. The results were compared with the 2D sample using model 1-c. In all cases, a nearly constant profile with an oscillating zone was observed at the neutral axis of the specimen which occurs because of the presence of a slip gradient but no slip. The GND density in the 3D specimen was approximately 10% higher, the difference can be attributed to the selected dimensions, that is, i.e. deviation in the boundary conditions can cause different behavior between 3D and 2D models (plane stress), especially close to the end of the cantilevered beam at which the X-symmetry condition was applied. Fig. 17 also compares different GND models in the 3D specimen. The differences were negligible (less than 1%). In addition, there was no significant difference in the computation time between all cases.

Finally, the homogenization method of the element was studied using the model 1-c. In this method, the gradient was computed in center of the element instead of calculating separately for each IP. A similar result with approximately 1% difference in the bent zone was obtained when homogenization was used. The only notable difference was that the homogenized solution exhibited fewer oscillations in the bent zone. Furthermore, no significant improvement in computation time (5% faster) was observed.

3.5. Polycrystal

In this section, we quantitatively investigate the absolute and relative error associated with the lattice incompatibility of different models. Numerous studies in literature investigated the grain size effect (Jiang et al., 1995; Counts et al., 2008; Zhang and Dong, 2016; Jiang et al., 2022; Agius et al., 2022; Demir et al., 2023b) using various CP-based finite element modeling approaches, but our intention here is slightly different: to examine the evolution of GND in the mid-grain of a RVE that possesses realistic stress states.

A polycrystal with 30 grains was generated using NEPER® software (Quey et al., 2011) and meshed with quadratic tetrahedral elements (C3D10) with four integration points per element. The mesh consisted of 165,968 elements. Each grain contained more than 1000 elements that is consistent with Lim et al. (2019) and the grain located in the center of the RVE (mid-grain) contains

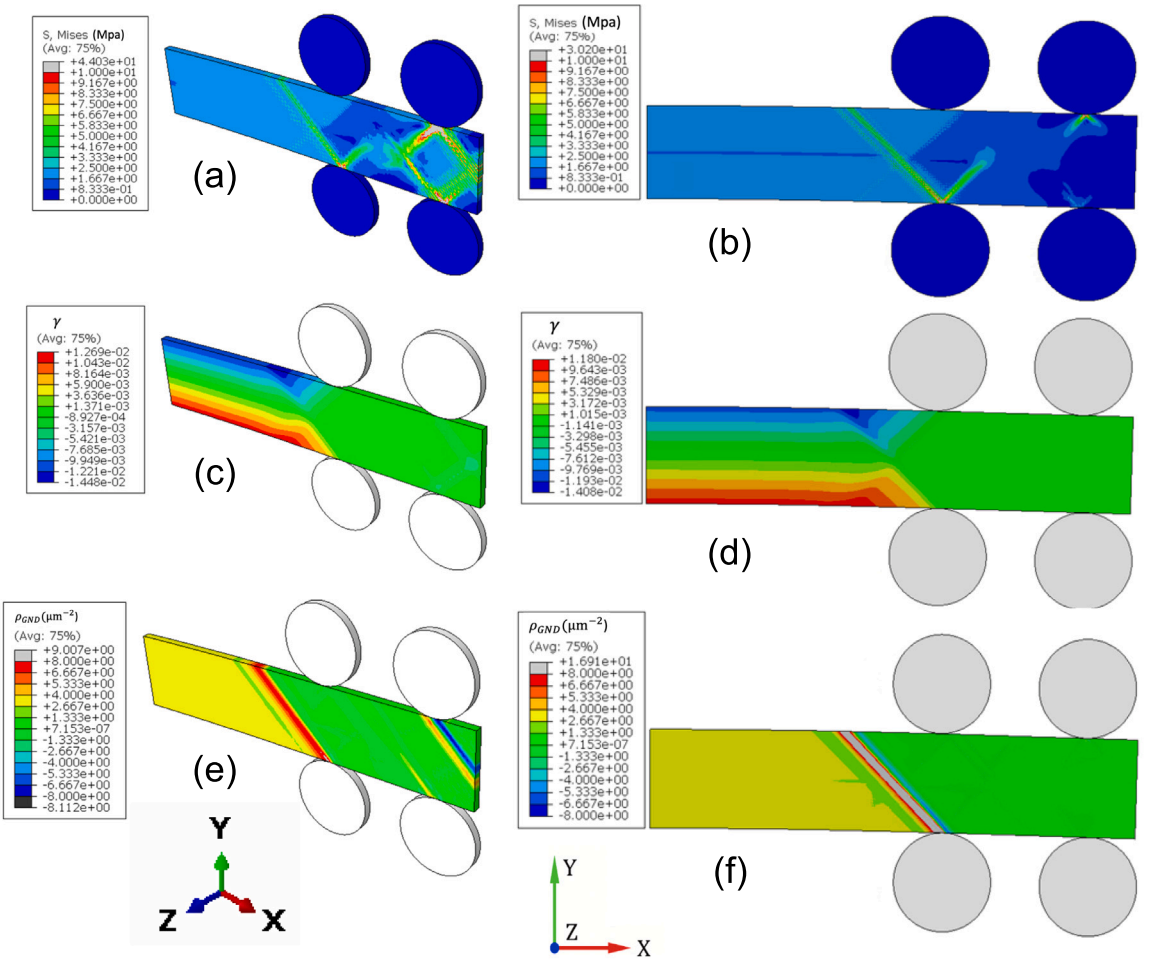

Fig. 16. von Mises stress distributions in (a) 3D and (b) 2D; total slip in (c) 3D and (d) 2D; GND density in (e) 3D and (f) 2D. GND model 1-c is used in the simulations.

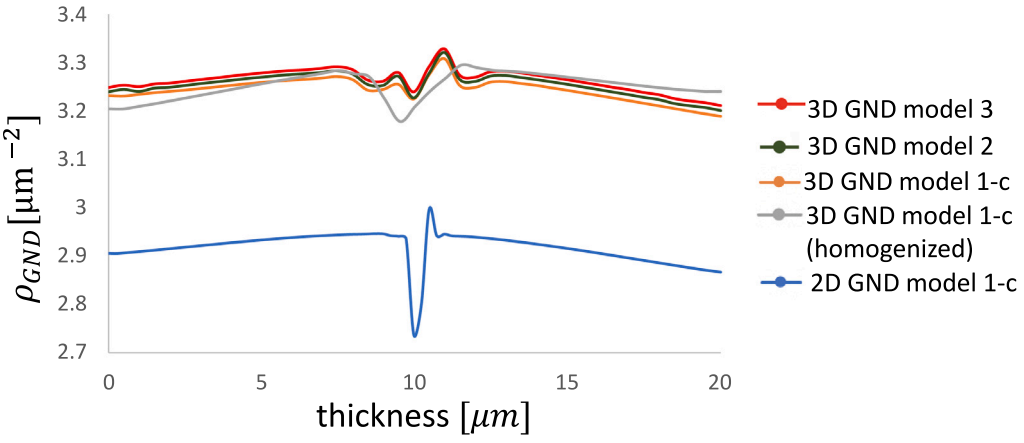

Fig. 17. GND density along thickness path for 2D and 3D simulation of four-point bending using model 1-c.

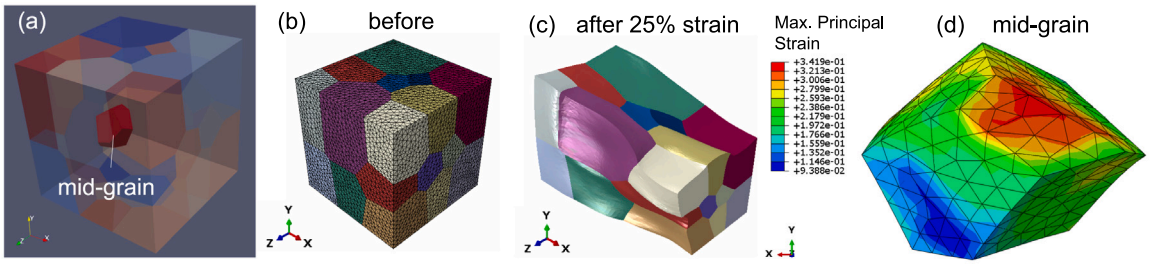

Fig. 18. (a) Polycrystal RVE with the mid-grain, (b) RVE and mesh before straining, (c) deformed geometry after 25% uniaxial strain, and (d) maximum principal true strain after 25% uniaxial strain for model 1-c (the models 1-d, 2, and 3 all are approximately 0.2% different hence not included.).

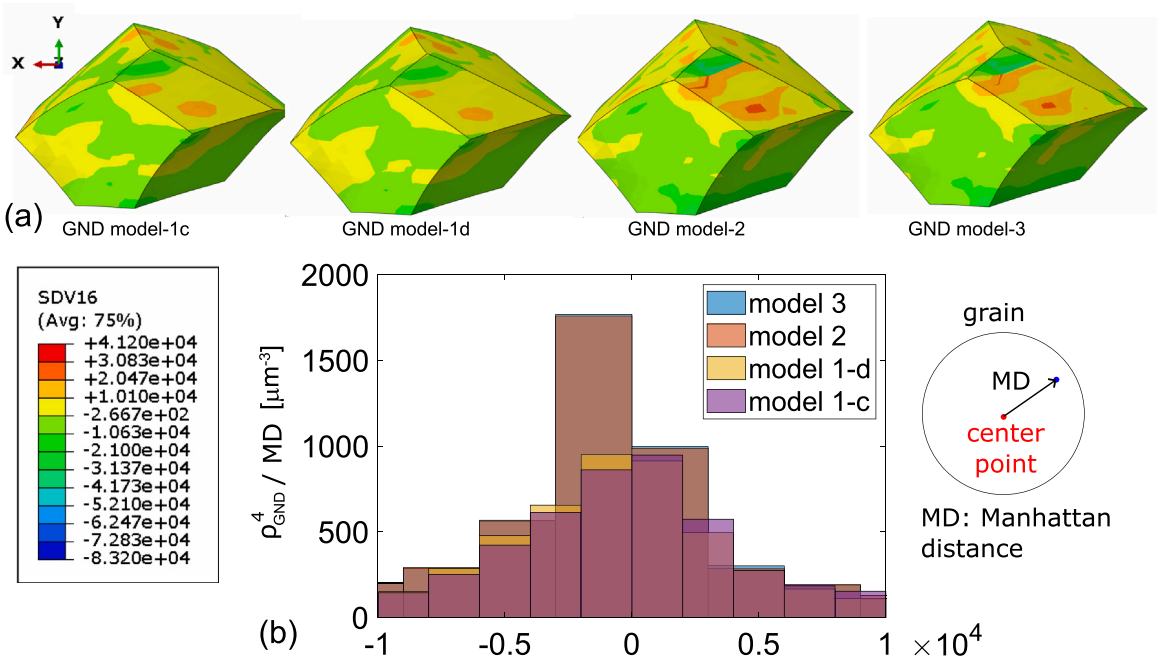

Fig. 19. Edge dislocation density in the most active slip system - 4, [110] $(\bar{1}11)$, in the mid-grain for four different GND models at the end of 25% uniaxial tension: (a) contour plots (legend is shown on the bottom left corner) and (b) Histogram of GND density (in the most active slip system - 4) normalized by Manhattan distance.

1,308 elements. A uniaxial macroscopic tensile strain of 25% was applied with a strain rate of 2.5×10^{-3} s^{-1}. GNDs were computed using the linear form of the shape functions for GND models 1-c, 1-d, 2, and 3. GND models 1-a and 1-b were excluded from this analysis based on the findings in Sections 3.1–3.4 because they give inconsistent results leading to significant amount of strain hardening and convergence issues.

Fig. 18 shows the polycrystal RVE with the center grain in which the effect of different GND models was investigated. Simulations were performed using a 2.4 GHz Intel E5-2680 v4 CPU on using a total of 20 threads. Simulation duration for models 1-c, 1-d, 2, and 3 were 41.09, 42.11, 37.01, and 37.03 hours, respectively. The simulation durations for the total form with and without deformed area correction (e.g., models 1-c and 1-d, respectively) was not significantly different from each other, similar to the simulation time for the models using the rate form and slip gradient (models 2 and 3). However, due to the inversion required to find the GND density using the SVD method, models 1-c and 1-d took approximately 14% longer than both the rate form and the slip gradient models in which the GND densities were obtained from simple vector projections.

Fig. 19 is obtained from the distribution of edge type of dislocations on the most active slip system (4th slip system $[01\bar{1}](01\bar{1})$) for comparison. Although the GND density distributions in Fig. 19(a) were quite the same on the surface plots, the GND density at the 5232 number of integration points of the mid-grain had a wide range of scatter. The average GND values were calculated as 2828, 2643, 3194, and 3102 μm^{-2} for models 1-c, 1-d, 2, and 3, respectively. The difference between model 1-d (which considers changes in area / dislocation flux with plastic deformation) with respect to model 1-c was approximately as 20% on average. Similarly, the GND density obtained by the rate form and the slip gradient (models 2 and 3) differs from the total form (model 1-c) by nearly

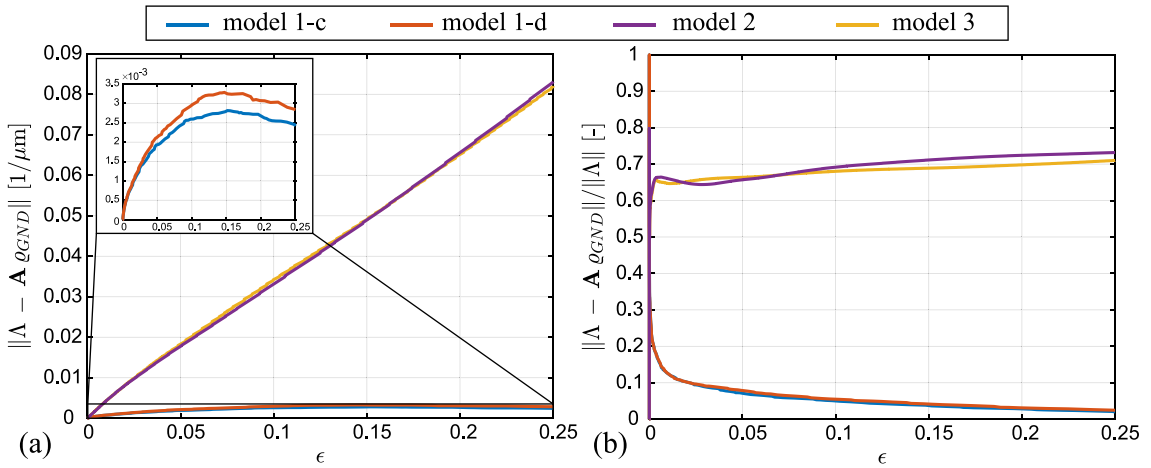

Fig. 20. Incompatibility error: (a) absolute and (b) relative average over the mid-grain vs. uniaxial strain for total form without area correction (model 1-c) and with area correction (model 1-d), rate form (model 2), and slip gradients (model 3). The relatively lower absolute errors for model 1-c and 1-d are presented within the subplot in part (a).

88%. Models 1-c and 1-d reveal the lowest average GND densities in the mid-grain which were closest to the minimum energy configuration making them the best approach.

The histogram plot in Fig. 19(b) shows the edge type GND density in slip system $[01\bar{1}](01\bar{1})$) normalized by the Manhattan distance. The GND density was normalized by the Manhattan distance to compensate for increasing numbers of integration or data points with increasing distance from the center of the grain to obtain a more representative histogram. The distribution was consistent for the models 1-c and 1-d as well as for models 2 and 3. The higher magnitude of GND density was concluded for models 2 and 3 compared to models 1-c and 1-d, that reveal solutions closer to minimum GND density hence a minimum eneergy configuration, suggesting better findings for models 1-c and 1-d.

The absolute and relative incompatibility errors were obtained by recalculation of incompatibility using the computed by GND densities with Nye's tensor. This error was a result of the effects of SVD inversion for the total forms, the neglected component of GND (edge dislocations along the slip plane normal), the accumulated errors in the rate form and the assumption of small strain for the slip gradients. The higher error in both of the rate forms is consistent with the findings in Levkovitch and Svendsen (2006).

Fig. 20 shows the comparison of the average norm of the incompatibility error that was obtained at all IPs in the mid grain using GND models 1-c, 1-d, 2, and 3. The absolute and relative errors associated with the rate form (model-2) and the slip gradient model (model-3) were greater relative to the total forms. The difference was approximately two orders of magnitude higher than that of both total forms (models 1-c and 1-d), which could be linked to the accumulation of numerical errors over time. In addition, neglecting the $\dot{\varrho}^a_{GND,en}$ term in Eq. (2.52) also contributes to this error. However, both total forms using a restricted solution to the active slip systems followed by SVD and inversion reveal relatively low differences, even though the error is averaged over the grain. The area correction reveals an additional 1.5% absolute error on average with respect to model 1-c while the relative errors were quite close between models 1-c and 1-d. Therefore, in an explicit GND calculation scheme, the total form of incompatibility measure appears to offer superior numerical accuracy rather than the rate forms because the total forms model 1-c or model 1-d reveal the least amount of error consistently representing the incompatibility.

In Fig. 20(b), the relative error initiates from the value of unity because of the initial threshold used for the GND densities. There was a small value of incompatibility present initially which did not exceed the GND density threshold thereby leaving GND density as zero and giving a relative error of unity (100% error), rather than zero at the start of the analysis.

Fig. 20 shows the average results over the mid-grain at which is the most representative location in a polycrystal because it has the most realistic stress state, uninfluenced by the boundary conditions defined at the edge of the FE model. The average error at the integration points becomes approximately zero for model 1-c and model 1-d for some IPs thus these models are most able to capture the incompatibility while providing physically realistic GND densities.

4. Conclusions

In this study, we investigate and compare several widely used incompatibility measures and GND calculation procedures in a crystal plasticity-based finite element framework. The important conclusions are outlined as follows:

- The total form of incompatibility, $(-\nabla\times\boldsymbol{F}_p)^T$ that has been used to compute GND densities in conjunction with the L2 method revealed GNDs on the inactive slip systems; leading to excessive and erratic strain hardening which also added solution convergence difficulty. The restriction of GNDs only to the active slip systems, followed by SVD and inversion allowed for a more physical calculation of GND density. The other rate form of incompatibility, $-\nabla\times\dot{\gamma}^a\,\boldsymbol{n}^a\,\boldsymbol{F}_p$, and that based on slip gradients, $\nabla\dot{\gamma}^a$, do not have this problem and always reveal GNDs on the active slip systems.

- A small numerical difference in the slip between the material points leads to formation and accumulation of fictitious GND densities. These artificial GNDs lead to misrepresentation of simple cases such as strain-gradient-free uniaxial tension of cube orientated single crystal under rotation-free symmetric loading. A threshold for the minimum value of the strain gradients is found to be essential for all of the GND methods investigated in this study which was overlooked in previous studies.
- Single crystal and single slip deformation cases of simple shear, uniaxial tension with and without strain gradients, and four-point bending were investigated to test the GND calculation method. The restriction of GND solution to the active slip systems have led to the more physically representative GND densities in all these cases that were in close agreement with the analytical solutions. The total form with solution restricted to active slip systems followed by SVD and inversion reveals very similar results to the rate form and the slip gradients at small deformations.
- Polycrystal simulations at large strains revealed significantly less densities for the total form than the rate form and slip gradients. This is due to the explicit calculation of GNDs for all the methods and incremental calculation leading to the error accumulation over time for the rate forms due to the redundancy in the definition of screw dislocations as explained in Levkovitch and Svendsen (2006).

Future studies will involve experimental validation of the theory presented by single crystal experiments that involve strain gradients such as micro cantilever beam bending and nanoindentation as well as polycyrstal tests in which strain gradients arise naturally due to anisotropy.

CRediT authorship contribution statement

Eralp Demir: Writing – review & editing, Writing – original draft, Software, Methodology, Conceptualization. **Alvaro Martinez-Pechero:** Writing – original draft, Visualization, Formal analysis. **Chris Hardie:** Writing – review & editing, Supervision, Methodology, Funding acquisition. **Edmund Tarleton:** Writing – review & editing, Writing – original draft, Supervision, Investigation, Funding acquisition.

Declaration of competing interest

The authors declare that they have no known competing financial interests or personal relationships that could have appeared to influence the work reported in this paper.

Data availability

We have provided public access to the code that was used to generate the data in this study (https://github.com/TarletonGroup/CrystalPlasticity).

Acknowledgments

We greatly appreciate the discussions with Prof. Fionn Dunne and his valuable comments on the strain gradient formulation. E. Tarleton acknowledges financial support from the Royal Academy of Engineering and UK Atomic Energy Authority (UKAEA) through a Senior Research Fellowship. A. M. Pechero acknowledges the support from the framework of the EUROfusion Consortium, funded by the European Union via the Euratom Research and Training Programme (Grant Agreement No. 12490 — EUROfusion) and from the EPSRC, United Kingdom (grant number R76251/CN001). We also acknowledge the STEP funding program of UKAEA.

Appendix A. Crystal to sample transformation

Crystal to sample transformation, $\boldsymbol{g}$, defines the passive transformation from the crystal to the sample reference frame, Eq. (A.1). $\boldsymbol{g}$ is computed by Bunge angles $(\varphi_1, \boldsymbol{\Phi}, \varphi_2)$.

$$\boldsymbol{g} = \begin{bmatrix} \cos\varphi_1 \cos\varphi_2 - \sin\varphi_1 \sin\varphi_2 \cos\boldsymbol{\Phi} & \sin\varphi_1 \cos\varphi_2 - \cos\varphi_1 \sin\varphi_2 \cos\boldsymbol{\Phi} & \sin\varphi_2 \sin\boldsymbol{\Phi} \\ -\cos\varphi_1 \sin\varphi_2 - \sin\varphi_1 \cos\varphi_2 \cos\boldsymbol{\Phi} & -\sin\varphi_1 \sin\varphi_2 + \cos\varphi_1 \cos\varphi_2 \cos\boldsymbol{\Phi} & \cos\varphi_2 \sin\boldsymbol{\Phi} \\ \sin\varphi_1 \sin\boldsymbol{\Phi} & -\cos\varphi_1 \sin\boldsymbol{\Phi} & \cos\boldsymbol{\Phi} \end{bmatrix}^T. \tag{A.1}$$

Appendix B. Curl of a second rank tensor

Let the line integral containing a vector field, $\boldsymbol{f}$ converts to a surface integral about a surface normal $\boldsymbol{r}$ by using Stoke's theorem gives Eq. (B.1):

$$\oint_L \boldsymbol{f} \cdot \mathbf{dx} = \int_S \nabla \times \boldsymbol{f} \cdot \boldsymbol{r}\, \mathrm{dA}. \tag{B.1}$$

Curl of a vector in index notation is given by Eq. (B.2) with Levi-Civita operator ε_{irs}:

$$\nabla \times \boldsymbol{f} = \varepsilon_{irs} f_{s,r}. \tag{B.2}$$

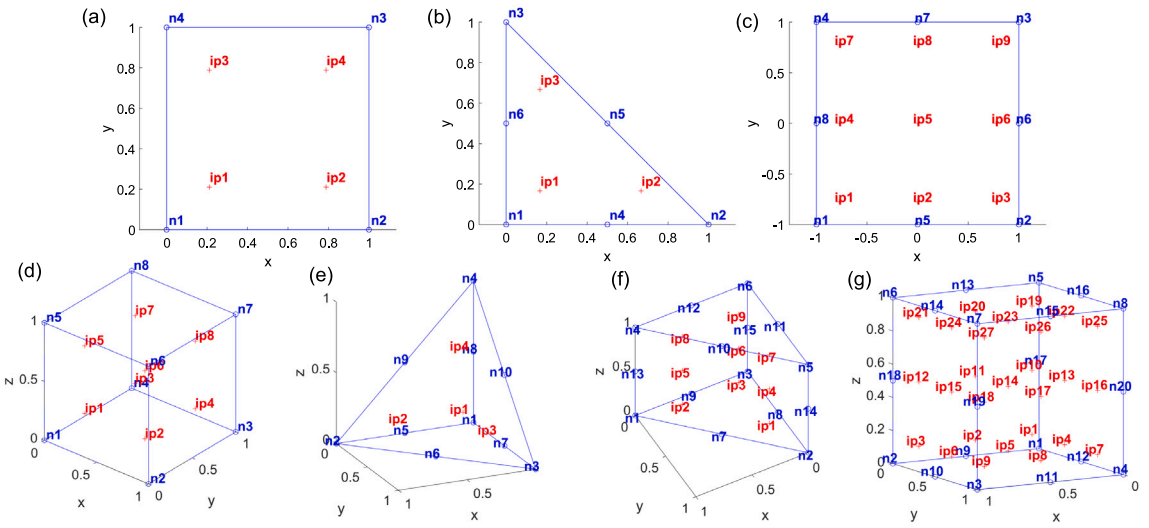

Fig. C.1. Node (n) and integration point (i) numbering of with full integration for different 2D and 3D element types: (a) linear quadrilateral, (b) quadratic triangular, (c) quadratic quadrilateral, (d) linear hexahedral, (e) quadratic tetrahedral, (f) quadratic triangular prism, (g) quadratic hexahedral.

Let the vector $\boldsymbol{f}$ is defined in terms of a constant vector $\boldsymbol{c}$ and a second rank tensor $\boldsymbol{T}$ in Eq. (B.3):

$$\boldsymbol{f} = \boldsymbol{c} \cdot \boldsymbol{T}. \tag{B.3}$$

such that it satisfies (B.1) as shown in Eq. (B.4):

$$\oint_L \boldsymbol{c} \cdot \boldsymbol{T} \cdot \mathbf{dx} = \int_S \nabla \times (\boldsymbol{c} \cdot \boldsymbol{T}) \cdot \boldsymbol{r}\, \mathrm{dA}. \tag{B.4}$$

Equating the curl of a vector in Eq. (B.2) and the curl expression in Eq. (B.4) gives Eq. (B.5):

$$\nabla \times \boldsymbol{f} = \nabla \times (\boldsymbol{c} \cdot \boldsymbol{T}). \tag{B.5}$$

which becomes as in Eq. (B.6) in index notation:

$$\varepsilon_{irs}\, f_{s,r} = c_j\, \varepsilon_{irs}\, T_{js,r}. \tag{B.6}$$

The right-hand-side of the Eq. (B.6) can be re-arranged to give Eq. (B.7):

$$\nabla \times (\boldsymbol{c} \cdot \boldsymbol{T}) = \left(\varepsilon_{irs}\, T_{js,r}\, \boldsymbol{e}_i \otimes \boldsymbol{e}_j\right) \cdot c_k\, \boldsymbol{e}_k. \tag{B.7}$$

Eq. (B.7) can be written in matrix notation together with the property of transpose giving Eq. (B.8):

$$\nabla \times (\boldsymbol{c} \cdot \boldsymbol{T}) = \nabla \times \left(\boldsymbol{T}^T \cdot \boldsymbol{c}\right) = (\nabla \times \boldsymbol{T}) \cdot \boldsymbol{c}. \tag{B.8}$$

Equating the expressions in Eqs. (B.7) and (B.8), the curl of a second rank tensor becomes as in Eq. (B.9);

$$(\nabla \times \boldsymbol{T})_{ij} = \varepsilon_{irs}\, T_{js,r}. \tag{B.9}$$

Appendix C. Element types and interpolation functions

Fig. C.1 shows different 2D and 3D element types used during the GND calculation.

C.1. 4-node linear quadrilateral elements (CPS4/CPE4)

$$\begin{aligned} N_1 &= (1-g)(1-h)/4, \quad N_2 = (1+g)(1-h)/4, \\ N_3 &= (1+g)(1+h)/4, \quad N_4 = (1-g)(1+h)/4. \end{aligned} \tag{C.1}$$

C.2. 6-node quadratic triangular elements (CPS6/CPE6)

$$N_1 = 2(1/2 - g - h)(1 - g - h), \quad N_2 = 2g(g - 1/2), \quad N_3 = 2h(h - 1/2),$$
$$N_4 = 4g(1 - g - h), \quad N_5 = 4gh, \quad N_6 = 4h(1 - g - h). \tag{C.2}$$

C.3. 8-node quadrilateral elements (CPS8/CPE8)

$$N_1 = -(1 - g)(1 - h)(1 + g + h)/4, \quad N_2 = -(1 + g)(1 - h)(1 - g + h)/4,$$
$$N_3 = -(1 + g)(1 + h)(1 - g - h)/4, \quad N_4 = -(1 - g)(1 + h)(1 + g - h)/4,$$
$$N_5 = (1 - g)(1 + g)(1 - h)/2, \quad N_6 = (1 - h)(1 + h)(1 + g)/2,$$
$$N_7 = (1 - g)(1 + g)(1 + h)/2, \quad N_8 = (1 - h)(1 + h)(1 - g)/2. \tag{C.3}$$

C.4. 8-node linear solid brick elements (C3D8)

$$N_1 = (1 - g)(1 - h)(1 - r)/8, \quad N_2 = (1 + g)(1 - h)(1 - r)/8,$$
$$N_3 = (1 + g)(1 + h)(1 - r)/8, \quad N_4 = (1 - g)(1 + h)(1 - r)/8,$$
$$N_5 = (1 - g)(1 - h)(1 + r)/8, \quad N_6 = (1 + g)(1 - h)(1 + r)/8,$$
$$N_7 = (1 + g)(1 + h)(1 + r)/8, \quad N_8 = (1 - g)(1 + h)(1 + r)/8. \tag{C.4}$$

C.5. 10-node quadratic tetrahedral elements (C3D10)

$$N_1 = (2(1 - g - h - r) - 1)(1 - g - h - r),$$
$$N_2 = (2g - 1)g, \quad N_3 = (2h - 1)h, \quad N_4 = (2r - 1)r,$$
$$N_5 = 4(1 - g - h - r)g, \quad N_6 = 4gh, \quad N_7 = 4(1 - g - h - r)h,$$
$$N_8 = 4(1 - g - h - r)r, \quad N_9 = 4gr, \quad N_{10} = 4hr. \tag{C.5}$$

C.6. 15-node quadratic wedge elements (C3D15)

$$N_1 = [(1 - g - h)(2(1 - g - h) - 1)(1 - r) - (1 - g - h)(1 - r^2)]/2,$$
$$N_2 = [g(2g - 1)(1 - r) - g(1 - r^2)]/2, \quad N_3 = [h(2h - 1)(1 - r) - h(1 - r^2)]/2,$$
$$N_4 = [(1 - g - h)(2(1 - g - h) - 1)(1 + r) - (1 - g - h)(1 - r^2)]/2,$$
$$N_5 = [g(2g - 1)(1 + r) - g(1 - r^2)]/2, \quad N_6 = [h(2h - 1)(1 + r) - h(1 - r^2)]/2,$$
$$N_7 = 2(1 - g - h)g(1 - r), \quad N_8 = 2gh(1 - r), \quad N_9 = 2h(1 - g - h)(1 - r),$$
$$N_{10} = 2(1 - g - h)g(1 + r), \quad N_{11} = 2gh(1 + r), \quad N_{12} = 2h(1 - g - h)(1 + r),$$
$$N_{13} = (1 - g - h)(1 - r^2), \quad N_{14} = g(1 - r^2), \quad N_{15} = h(1 - r^2). \tag{C.6}$$

C.7. 20-node quadratic solid brick elements (C3D20)

$$N_1 = (g - 1)/8(h - 1)(r - 1)(g + h + r + 2), \quad N_2 = -(g + 1)/8(h - 1)(r - 1)(h - g + r + 2),$$
$$N_3 = -(g + 1)/8(h + 1)(r - 1)(g + h - r - 2), \quad N_4 = -(g - 1)/8(h + 1)(r - 1)(g - h + r + 2),$$
$$N_5 = -(g - 1)/8(h - 1)(r + 1)(g + h - r + 2), \quad N_6 = -(g + 1)/8(h - 1)(r + 1)(g - h + r - 2),$$
$$N_7 = (g + 1)/8(h + 1)(r + 1)(g + h + r - 2), \quad N_8 = (g - 1)/8(h + 1)(r + 1)(g - h - r + 2),$$
$$N_9 = -(g - 1)/4(g + 1)(h - 1)(r - 1), \quad N_{10} = (h - 1)/4(g + 1)(h + 1)(r - 1),$$
$$N_{11} = (g - 1)/4(g + 1)(h + 1)(r - 1), \quad N_{12} = -(h - 1)/4(g - 1)(h + 1)(r - 1),$$
$$N_{13} = (g - 1)/4(g + 1)(h - 1)(r + 1), \quad N_{14} = -(h - 1)/4(g + 1)(h + 1)(r + 1),$$

$$N_{15} = -(g-1)/4\,(g+1)\,(h+1)\,(r+1), \quad N_{16} = (h-1)/4\,(g-1)\,(h+1)\,(r+1),$$
$$N_{17} = -(r-1)/4\,(g-1)\,(h-1)\,(r+1), \quad N_{18} = (r-1)/4\,(g+1)\,(h-1)\,(r+1),$$
$$N_{19} = -(r-1)/4\,(g+1)\,(h+1)\,(r+1), \quad N_{20} = (r-1)/4\,(g-1)\,(h+1)\,(r+1). \tag{C.7}$$

References

Acharya, A., Bassani, J., 2000. Lattice incompatibility and a gradient theory of crystal plasticity. J. Mech. Phys. Solids 48 (8), 1565–1595.

Agius, D., Kareer, A., Al Mamun, A., Truman, C., Collins, D.M., Mostafavi, M., Knowles, D., 2022. A crystal plasticity model that accounts for grain size effects and slip system interactions on the deformation of austenitic stainless steels. Int. J. Plast. 152, 103249.

Arora, R., Zhang, X., Acharya, A., 2020. Finite element approximation of finite deformation dislocation mechanics. Comput. Methods Appl. Mech. Engrg. 367, 113076.

Arsenlis, A., Parks, D., 1999. Crystallographic aspects of geometrically-necessary and statistically-stored dislocation density. Acta Mater. 47 (5), 1597–1611.

Asaro, R.J., 1983. Crystal plasticity. J. Appl. Mech. 50 (4b), 921–934.

Bandyopadhyay, R., Gustafson, S.E., Kapoor, K., Naragani, D., Pagan, D.C., Sangid, M.D., 2021. Comparative assessment of backstress models using high-energy X-ray diffraction microscopy experiments and crystal plasticity finite element simulations. Int. J. Plast. 136, 102887.

Birosca, S., Liu, G., Ding, R., Jiang, J., Simm, T., Deen, C., Whittaker, M., 2019. The dislocation behaviour and GND development in a nickel based superalloy during creep. Int. J. Plast. 118, 252–268.

Bond, W.L., 1943. The mathematics of the physical properties of crystals. Bell Syst. Tech. J. 22 (1), 1–72.

Busso, E., Meissonnier, F., O'dowd, N., 2000. Gradient-dependent deformation of two-phase single crystals. J. Mech. Phys. Solids 48 (11), 2333–2361.

Cermelli, P., Gurtin, M.E., 2001. On the characterization of geometrically necessary dislocations in finite plasticity. J. Mech. Phys. Solids 49 (7), 1539–1568.

Chen, B., Jiang, J., Dunne, F.P., 2017. Microstructurally-sensitive fatigue crack nucleation in Ni-based single and oligo crystals. J. Mech. Phys. Solids 106, 15–33.

Clayton, J.D., McDowell, D.L., Bammann, D.J., 2004. A multiscale gradient theory for single crystalline elastoviscoplasticity. Int. J. Eng. Sci. 42 (5–6), 427–457.

Counts, W.A., Braginsky, M.V., Battaile, C.C., Holm, E.A., 2008. Predicting the Hall–Petch effect in fcc metals using non-local crystal plasticity. Int. J. Plast. 24 (7), 1243–1263.

Dai, H., 1997. Geometrically-Necessary Dislocation Density in Continuum Plasticity Theory, fem Implementation and Applications (Ph.D. thesis). Massachusetts Institute of Technology.

Das, S., Hofmann, F., Tarleton, E., 2018. Consistent determination of geometrically necessary dislocation density from simulations and experiments. Int. J. Plast. 109, 18–42.

Demir, E., Horton, E.W., Kareer, A., Collins, D.M., Mostafavi, M., Knowles, D., 2023a. A finite element method to calculate geometrically necessary dislocation density: Accounting for orientation discontinuities in polycrystals. Acta Mater. 245, 118658.

Demir, E., Horton, E.W., Mokhtarishirazabad, M., Mostafavi, M., Knowles, D., 2023b. Grain size and shape dependent crystal plasticity finite element model and its application to electron beam welded SS316L. J. Mech. Phys. Solids 105331.

Demir, E., Raabe, D., Zaafarani, N., Zaefferer, S., 2009. Investigation of the indentation size effect through the measurement of the geometrically necessary dislocations beneath small indents of different depths using EBSD tomography. Acta Mater. 57 (2), 559–569.

Dunne, F., Rugg, D., Walker, A., 2007. Lengthscale-dependent, elastically anisotropic, physically-based hcp crystal plasticity: Application to cold-dwell fatigue in Ti alloys. Int. J. Plast. 23 (6), 1061–1083.

El-Dasher, B., Adams, B., Rollett, A., 2003. Experimental recovery of geometrically necessary dislocation density in polycrystals. Scr. Mater. 48 (2), 141–145.

Erinosho, T., Dunne, F., 2014. Lattice strain distributions due to elastic distortions and GND development in polycrystals. J. Mech. Phys. Solids 67, 62–86.

Evers, L., Brekelmans, W., Geers, M., 2004. Non-local crystal plasticity model with intrinsic SSD and GND effects. J. Mech. Phys. Solids 52 (10), 2379–2401.

Fleck, N., Muller, G., Ashby, M.F., Hutchinson, J.W., 1994. Strain gradient plasticity: theory and experiment. Acta Metall. Mater. 42 (2), 475–487.

Gao, P., Fei, M., Zhan, M., Fu, M., 2023. Microstructure-and damage-nucleation-based crystal plasticity finite element modeling for the nucleation of multi-type voids during plastic deformation of al alloys. Int. J. Plast. 165, 103609.

Gerken, J.M., Dawson, P.R., 2008. A crystal plasticity model that incorporates stresses and strains due to slip gradients. J. Mech. Phys. Solids 56 (4), 1651–1672.

Gurtin, M.E., 2000. On the plasticity of single crystals: free energy, microforces, plastic-strain gradients. J. Mech. Phys. Solids 48 (5), 989–1036.

Hill, R., Rice, J., 1972. Constitutive analysis of elastic-plastic crystals at arbitrary strain. J. Mech. Phys. Solids 20 (6), 401–413.

Hull, D., Bacon, D.J., 2011. Introduction to Dislocations, vol. 37, Elsevier.

Jiang, J., Britton, T.B., Wilkinson, A.J., 2015. The orientation and strain dependence of dislocation structure evolution in monotonically deformed polycrystalline copper. Int. J. Plast. 69, 102–117.

Jiang, M., Fan, Z., Kruch, S., Devincre, B., 2022. Grain size effect of FCC polycrystal: A new CPFEM approach based on surface geometrically necessary dislocations. Int. J. Plast. 150, 103181.

Jiang, Z., Lian, J., Baudelet, B., 1995. A dislocation density approximation for the flow stress—grain size relation of polycrystals. Acta Metall. Mater. 43 (9), 3349–3360.

Klusemann, B., Yalçinkaya, T., 2013. Plastic deformation induced microstructure evolution through gradient enhanced crystal plasticity based on a non-convex Helmholtz energy. Int. J. Plast. 48, 168–188.

Konijnenberg, P.J., Zaefferer, S., Raabe, D., 2015. Assessment of geometrically necessary dislocation levels derived by 3D EBSD. Acta Mater. 99, 402–414.

Kuhn, H.W., Tucker, A.W., J., N., 1951. Proceedings of the second berkeley symposium on mathematical statistics and probability. In: Nonlinear Programming. Berkeley and Los Angeles, University of California Press, pp. 481–492.

Kuksenko, V., Roberts, S., Tarleton, E., 2019. The hardness and modulus of polycrystalline beryllium from nano-indentation. Int. J. Plast. 116, 62–80.

Kuroda, M., 2011. On large-strain finite element solutions of higher-order gradient crystal plasticity. Int. J. Solids Struct. 48 (24), 3382–3394.

Kuroda, M., Tvergaard, V., 2008. A finite deformation theory of higher-order gradient crystal plasticity. J. Mech. Phys. Solids 56 (8), 2573–2584.

Kysar, J., Saito, Y., Oztop, M., Lee, D., Huh, W., 2010. Experimental lower bounds on geometrically necessary dislocation density. Int. J. Plast. 26 (8), 1097–1123.

Levkovitch, V., Svendsen, B., 2006. On the large-deformation-and continuum-based formulation of models for extended crystal plasticity. Int. J. Solids Struct. 43 (24), 7246–7267.

Li, F.-F., Fang, G., 2020. Modeling of 3D plastic anisotropy and asymmetry of extruded magnesium alloy and its applications in three-point bending. Int. J. Plast. 130, 102704.

Li, K., Tang, B., Zhang, M., Zhao, L., Liu, X., Fan, J., Li, J., 2023. A hydrogen diffusion model considering grain boundary characters based on crystal plasticity framework. Int. J. Plast. 169, 103740.

Lim, H., Battaile, C.C., Bishop, J.E., Foulk, III, J.W., 2019. Investigating mesh sensitivity and polycrystalline RVEs in crystal plasticity finite element simulations. Int. J. Plast. 121, 101–115.

Lyu, H., Ruimi, A., Zbib, H.M., 2015. A dislocation-based model for deformation and size effect in multi-phase steels. Int. J. Plast. 72, 44–59.

Ma, A., Roters, F., Raabe, D., 2006. A dislocation density based constitutive model for crystal plasticity FEM including geometrically necessary dislocations. Acta Mater. 54 (8), 2169–2179.
Marano, A., Gélébart, L., Forest, S., 2019. Intragranular localization induced by softening crystal plasticity: Analysis of slip and kink bands localization modes from high resolution FFT-simulations results. Acta Mater. 175, 262–275.
Nye, J.F., 1953. Some geometrical relations in dislocated crystals. Acta Metall. 1 (2), 153–162.
Pai, N., Prakash, A., Samajdar, I., Patra, A., 2022. Study of grain boundary orientation gradients through combined experiments and strain gradient crystal plasticity modeling. Int. J. Plast. 156, 103360.
Pantleon, W., 2008. Resolving the geometrically necessary dislocation content by conventional electron backscattering diffraction. Scr. Mater. 58 (11), 994–997.
Pouriayevali, H., Xu, B.-X., 2017. Decomposition of dislocation densities at grain boundary in a finite-deformation gradient crystal-plasticity framework. Int. J. Plast. 96, 36–55.
Prastiti, N.G., Xu, Y., Balint, D.S., Dunne, F.P., 2020. Discrete dislocation, crystal plasticity and experimental studies of fatigue crack nucleation in single-crystal nickel. Int. J. Plast. 126, 102615.
Quey, R., Dawson, P., Barbe, F., 2011. Large-scale 3D random polycrystals for the finite element method: Generation, meshing and remeshing. Comput. Methods Appl. Mech. Engrg. 200 (17–20), 1729–1745.
Ramazani, A., Mukherjee, K., Schwedt, A., Goravanchi, P., Prahl, U., Bleck, W., 2013. Quantification of the effect of transformation-induced geometrically necessary dislocations on the flow-curve modelling of dual-phase steels. Int. J. Plast. 43, 128–152.
Reuber, C., Eisenlohr, P., Roters, F., Raabe, D., 2014. Dislocation density distribution around an indent in single-crystalline nickel: Comparing nonlocal crystal plasticity finite-element predictions with experiments. Acta Mater. 71, 333–348.
Roters, F., Eisenlohr, P., Kords, C., Tjahjanto, D.D., Diehl, M., Raabe, D., 2012. DAMASK: the Düsseldorf advanced material simulation kit for studying crystal plasticity using an FE based or a spectral numerical solver. Procedia Iutam 3, 3–10.
Ruggles, T., Fullwood, D., Kysar, J., 2016. Resolving geometrically necessary dislocation density onto individual dislocation types using EBSD-based continuum dislocation microscopy. Int. J. Plast. 76, 231–243.
Ryś, M., Forest, S., Petryk, H., 2020. A micromorphic crystal plasticity model with the gradient-enhanced incremental hardening law. Int. J. Plast. 128, 102655.
Sedaghat, O., Abdolvand, H., 2021. A non-local crystal plasticity constitutive model for hexagonal close-packed polycrystals. Int. J. Plast. 136, 102883.
Stupkiewicz, S., Petryk, H., 2016. A minimal gradient-enhancement of the classical continuum theory of crystal plasticity. Part II: Size effects. Arch. Mech. 68 (6), 487–513.
Sun, F., Meade, E.D., O'Dowd, N.P., 2019. Strain gradient crystal plasticity modelling of size effects in a hierarchical martensitic steel using the Voronoi tessellation method. Int. J. Plast. 119, 215–229.
Sun, F., Wang, S., Xie, Q., 2022. Role of particles and lattice rotation in tension–compression asymmetry of aluminium alloys. Int. J. Plast. 159, 103464.
Tang, X., Wang, Z., Wang, X., Deng, L., Zhang, M., Gong, P., Jin, J., Fu, M., 2023. Unraveling size-affected plastic heterogeneity and asymmetry during micro-scaled deformation of CP-Ti by non-local crystal plasticity modeling. Int. J. Plast. 170, 103733.
Tarleton, E., 2023. Github link for crystal plasticity code. https://github.com/TarletonGroup/CrystalPlasticity. (Accessed 18 October 2023).
Wilkinson, A.J., Meaden, G., Dingley, D.J., 2006. High-resolution elastic strain measurement from electron backscatter diffraction patterns: New levels of sensitivity. Ultramicroscopy 106 (4–5), 307–313.
Witzen, W.A., Polonsky, A.T., Pollock, T.M., Beyerlein, I.J., 2020. Three-dimensional maps of geometrically necessary dislocation densities in additively manufactured Ni-based superalloy IN718. Int. J. Plast. 131, 102709.
Xiao, X., Chen, L., Yu, L., Duan, H., 2019. Modelling nano-indentation of ion-irradiated FCC single crystals by strain-gradient crystal plasticity theory. Int. J. Plast. 116, 216–231.
Xu, Y., 2021a. A non-local methodology for geometrically necessary dislocations and application to crack tips. Int. J. Plast. 140, 102970.
Xu, Y., 2021b. A non-local methodology for geometrically necessary dislocations and application to crack tips. Int. J. Plast. 140, 102970.
Zan, X., Guo, X., Weng, G., Chen, G., 2023. Nanoindentation study of δ-phase zirconium hydride using the crystal plasticity model. Int. J. Plast. 103675.
Zhang, H., Dong, X., 2015. Physically based crystal plasticity FEM including geometrically necessary dislocations: numerical implementation and applications in micro-forming. Comput. Mater. Sci. 110, 308–320.
Zhang, H., Dong, X., 2016. Experimental and numerical studies of coupling size effects on material behaviors of polycrystalline metallic foils in microscale plastic deformation. Mater. Sci. Eng. A 658, 450–462.
Zhang, X., Zhao, J., Kang, G., Zaiser, M., 2023. Geometrically necessary dislocations and related kinematic hardening in gradient grained materials: A nonlocal crystal plasticity study. Int. J. Plast. 163, 103553.
Zhu, C., Livescu, V., Harrington, T., Dippo, O., Gray, III, G.T., Vecchio, K.S., 2017. Investigation of the shear response and geometrically necessary dislocation densities in shear localization in high-purity titanium. Int. J. Plast. 92, 148–163.